

Thermal conduction and thermopower of inner crusts of magnetized neutron stars

Henrik Danielyan,^{1,*} Arus Harutyunyan,^{2,1,†} and Armen Sedrakian^{3,4,‡}

¹*Physics Institute, Yerevan State University, Yerevan 0025, Armenia*

²*Byurakan Astrophysical Observatory, Byurakan 0213, Armenia*

³*Frankfurt Institute for Advanced Studies, D-60438 Frankfurt am Main, Germany*

⁴*Institute of Theoretical Physics, University of Wrocław, 50-204 Wrocław, Poland*

We compute the thermal conductivity and thermoelectric power (thermopower) of the inner crust of compact stars across a broad temperature–density domain relevant for proto–neutron stars, binary neutron-star mergers, and accreting neutron stars. The analysis covers the transition from a semi-degenerate to a highly degenerate electron gas and assumes temperatures above the melting threshold of the nuclear lattice, such that nuclei form a liquid. The transport coefficients are obtained by solving the Boltzmann kinetic equation in the relaxation-time approximation, fully incorporating the anisotropies generated by non-quantizing magnetic fields. Electron scattering rates include (i) dynamical screening of the electron–ion interaction in the hard-thermal-loop approximation of QED, (ii) ion–ion correlations within a one-component plasma, and (iii) finite nuclear-size effects. As an additional refinement, we evaluate electron–neutron scattering induced by the coupling of electrons to the anomalous magnetic moment of free neutrons; this contribution is found to be subdominant throughout the parameter range explored. To assess the sensitivity of transport coefficients to the underlying microphysics, we perform calculations for several inner-crust compositions obtained from different nuclear interactions and many-body methods. Across most of the crust, variations in relaxation times and in the components of the anisotropic thermal-conductivity and thermopower tensors reach up to factors $3 \div 4$ and $1.5 \div 2$, respectively, with the exception of the region where pasta phases are expected. These results provide updated, composition-dependent microphysical inputs for dissipative magneto-hydrodynamic simulations of warm neutron stars and post-merger remnants, where anisotropic heat and charge transport are of critical importance.

PACS numbers:

I. INTRODUCTION

Transport coefficients of cold and dense plasma in neutron stars, both in the liquid and solid phases have been extensively studied for many decades [1–13] (see Refs. [14, 15] for reviews). More recently, the transport in high-temperature regime, where transition from cold, degenerate matter to semi-degenerate or non-degenerate plasma might occur, has become of great interest. The dense nuclear matter in a heated plasma state is relevant mainly to binary neutron star mergers, proto-neutron stars, and neutron stars accreting matter from a companion. In this process, matter is expected to be heated to temperatures of the order of 100 MeV, likely featuring large thermal and compositional gradients and strong electromagnetic fields.

The primary focus of our work is the transport properties of the *inner crust* of neutron stars, where ultra-relativistic electrons, heavy nuclei, and a Fermi gas of unbound neutrons coexist. In this region, electrons dominate both charge and heat transport, as the contribution of normal (non-superfluid) neutrons to the thermal conductivity is known to be negligible [16]. A detailed calculation of the electrical conductivity in this inner-crust

regime was recently carried out in Ref. [17]. Complementary studies of *outer-crust* matter – including the electrical and thermal conductivities of hot, dense, fully ionized plasmas – were performed in Refs. [18, 19]. The electrical conductivity results of Ref. [18] were subsequently used to quantify the roles of Ohmic dissipation and the Hall effect in binary neutron-star mergers [20], and to delineate the parameter space in which a magnetohydrodynamic treatment remains valid. These outer-crust studies provide a useful reference, while the more recent extension to the inner crust [17] addresses the additional microphysics introduced by the presence of free neutrons and heavier nuclear clusters.

The dominant scattering channel, which determines the electron transport in the inner crust, is the Coulomb scattering off the ions. However, electron-neutron interaction via the coupling of the electron to the neutron’s anomalous magnetic moment has also been studied. Refs. [1, 21] considered the low-temperature regime where the neutron star matter is in a solid state in the crust or forms a Fermi-liquid in the core. It was found that the effect of electron-neutron scattering on the thermal conductivity is small in the inner crust [1], but can become important in the core [21]. Ref. [22] studied the induced electron-neutron interaction due to ions (in the inner crust) or protons (in the core), and found that the contribution of this interaction to transport coefficients is always negligible in the inner crust.

In the presence of magnetic fields, the conduction in the crust becomes anisotropic, and the transport in the

*Electronic address: danielyanhenri@gmail.com

†Electronic address: arus@bao.sci.am

‡Electronic address: sedrakian@fias.uni-frankfurt.de

direction transverse to the magnetic field becomes suppressed. Additionally, the simultaneous presence of electromagnetic fields and thermal gradients mixes various transport channels, leading to coupled non-trivial dynamics in the evolution of temperature and magnetic field profiles. In particular, a generation mechanism of strong magnetic fields via the dynamo effect (*i.e.*, magnetic field amplification) driven by strong thermal gradients was proposed earlier in Refs. [23–27]. Thermoelectric and thermomagnetic effects have also been considered in the context of thermal evolution of neutron stars [28–31].

In this work, we will compute the thermal conductivity and the thermoelectric power (thermopower) in the inner crust of a moderately warm neutron star, including the anisotropies of the transport induced by strong magnetic fields below the quantization limit $B \leq 10^{14}$ G. We will extend the formalism developed previously for assessment of electrical and thermal conductivities in the outer crust [18, 19] to the inner crust, adopting five composition models for spherical nuclei [32–35], which were employed recently to compute the electrical conductivity of the same system in Ref. [17].

In the regime relevant to this work, the ions constitute a classical liquid, and ion–ion correlations are incorporated through the structure factor of a classical one-component plasma. In addition to electron–ion scattering, we also include the full finite-temperature scattering rate of electrons off neutrons via the neutron’s anomalous magnetic moment. Although earlier studies concluded that electron–neutron scattering is negligible [1], those calculations were performed assuming exchange of longitudinally screened plasmons with Debye screening. As we show below, the dominant contribution instead arises from the exchange of transversely screened plasmons. The longitudinal and transverse components of the photon polarization tensor are evaluated within the hard-thermal-loop (HTL) effective field theory [18, 36, 37]. Finally, we provide an order-of-magnitude estimates for the evolution timescales of crustal magnetic fields and identify the conditions under which thermoelectric effects may play a significant role in their dynamics.

This work is organized as follows. Section II discusses briefly the physical conditions in the inner crust of a neutron star for five different compositions employed in this work. Section III provides the derivation of the tensors of electrical and thermal conductivities and thermopower in magnetic fields from the Boltzmann equation. Section IV presents the numerical results for the thermal conductivity, thermopower, and magnetic field evolution timescales in the density, temperature, and B -field regimes of interest. Our results are summarized in Section V. Appendix A derives the electron-neutron scattering matrix element in a thermal medium, and Appendix B computes the resulting electron relaxation time. Appendix C collects the low-temperature formulae for the thermoelectric coefficients. We use the natural units with $\hbar = c = k_B = k_e = 1$, and the metric signature $(1, -1, -1, -1)$.

II. PHYSICAL CONDITIONS IN INNER CRUST

The inner crust of a neutron star consists of relativistic electrons, fully ionized nuclei, and a gas of unbound neutrons that emerges once the density exceeds the neutron-drip threshold. The total baryon density in the inner crust is then given by

$$n_B = An_i + (1 - V_N n_i)n_n, \quad (1)$$

where n_i and n_n are the number densities of ions and unbound neutrons, respectively, V_N is the volume of the nucleus, and $V_N n_i$ is the excluded volume correction [38]. The state of ions in the crust is characterized by the plasma parameter

$$\Gamma = \frac{e^2 Z^2}{T R_{\text{WS}}}, \quad (2)$$

where e is the elementary charge, Z is the ion charge number, T is the temperature, $R_{\text{WS}} = (4\pi n_i/3)^{-1/3}$ is the radius of the spherical volume per ion, *i.e.*, that of the Wigner-Seitz cell. Ions form a weakly coupled Boltzmann gas for $\Gamma \ll 1$, a strongly coupled liquid for $1 \leq \Gamma \leq \Gamma_m \simeq 160$, and a solid for $\Gamma > \Gamma_m$. The melting temperature of the crust is defined as $T_m = (e^2 Z^2)/(\Gamma_m R_{\text{WS}})$. The current study applies to the intermediate temperatures where the plasma is in a liquid state.

For numerical computations, we will adopt five different density-dependent compositions of crustal matter, which we label as NV [32], D1M and D1M* [33], Bsk24 [34], and Sly9 [35]. Although these compositions were computed at $T = 0$, we will assume in this work that they depend weakly on the temperature and remain valid up to the temperature $T = 10$ MeV, postponing the investigation of temperature-dependent compositions to future work. The key properties of these compositions, such as the nuclear charge Z , mass number A , and the fraction of unbound neutrons $Y_n = n_n/n$, where n_n and n are the neutron and total number densities, were analyzed and compared extensively in Ref. [17]. For completeness, we summarize the main features here.

The primary distinctions among the five compositions stem from differences in the predicted mass number A at high densities, specifically in the range $13.5 \leq \log_{10} \rho [\text{g cm}^{-3}] \leq 14$, where ρ denotes the matter mass density. The D1M and D1M* models yield comparatively large nuclei, with $300 \leq A \leq 2000$, accompanied by a low free-neutron fraction $0.7 \geq Y_n \geq 0.2$ in this density interval. In contrast, the Bsk24 and Sly9 models predict much smaller nuclei with $A \sim 200$ and a correspondingly higher neutron fraction $Y_n \sim 0.8$. The NV composition shows an intermediate behavior between these two classes for $\log_{10} \rho [\text{g cm}^{-3}] \geq 13.5$.

Figure 1 shows the ratio of the radius r_c of the nucleus in the ground state to that of the Wigner-Seitz cell, as well as the free-volume fraction for neutrons, $(1 - V_N n_i)$, as a functions of density. At high densities the D1M and D1M* models predict extremely large

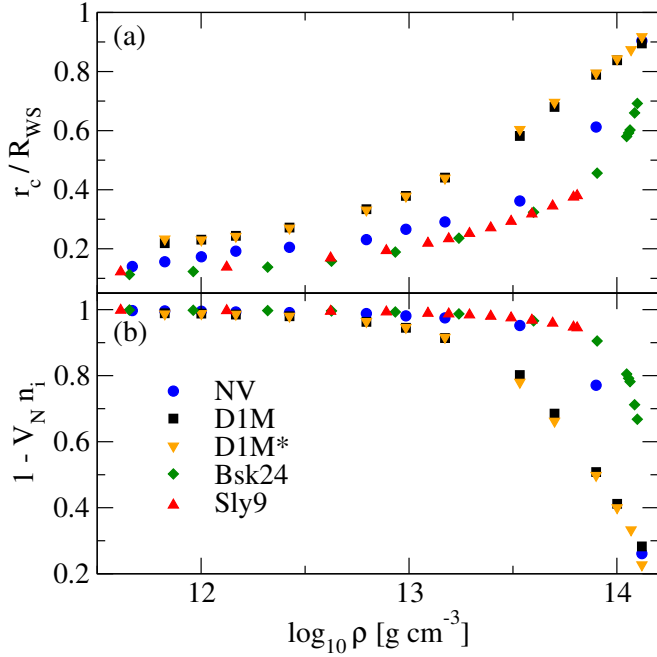


FIG. 1: (a) The ratio of the nucleus radius r_c to that of the Wigner-Seitz cell and (b) the volume fraction $(1 - V_N n_i)$ occupied by neutron gas as functions of density for five compositions of stellar matter.

nuclei that occupy a substantial fraction of the cell volume. Consequently, these models leave significantly less available volume for the free-neutron component compared with the other compositions. In the regime of interest, electrons form a degenerate or semi-degenerate ultrarelativistic Fermi gas, with the Fermi energy given by $\epsilon_F = (p_F^2 + m_e^2)^{1/2} \geq 25$ MeV, $p_F = (3\pi^2 n_e)^{1/3}$, where $n_e = Zn_i$ is the electron density, p_F – the Fermi momentum, and m_e – the electron (vacuum) mass.

III. THERMOELECTRIC TRANSPORT FROM THE BOLTZMANN EQUATION

A. Solving the Boltzmann equation

In this work, we mainly follow Refs. [18, 19] to present the Boltzmann framework for thermoelectric transport in the presence of magnetic fields. The electron dynamics is governed by the Boltzmann equation for the electron distribution function

$$\frac{\partial f}{\partial t} + \mathbf{v} \frac{\partial f}{\partial \mathbf{r}} - e(\mathbf{E} + \mathbf{v} \times \mathbf{B}) \frac{\partial f}{\partial \mathbf{p}} = I, \quad (3)$$

where \mathbf{E} and \mathbf{B} are the electric and magnetic fields, $\mathbf{v} = \partial \epsilon / \partial \mathbf{p}$ is the electron velocity with $\epsilon = \sqrt{p^2 + m_e^2}$, e is the unit charge, and $I = I_{ei} + I_{en}$ is the collision integral which includes the electron-ion and electron-neutron

scattering processes. These integrals are given by

$$I_{ei} = -(2\pi)^4 \sum_{234} |\mathcal{M}_{12 \rightarrow 34}^{ei}|^2 \delta^{(4)}(p_1 + p_2 - p_3 - p_4) \times [f_1(1 - f_3)g_2 - f_3(1 - f_1)g_4], \quad (4)$$

$$I_{en} = -(2\pi)^4 \sum_{234} |\mathcal{M}_{12 \rightarrow 34}^{en}|^2 \delta^{(4)}(p_1 + p_2 - p_3 - p_4) \times [f_1(1 - f_3)f'_2(1 - f'_4) - f_3(1 - f_1)f'_4(1 - f'_2)], \quad (5)$$

where (using short-hand notation) $f_{1,3} \equiv f(p_{1,3})$ and $f'_{2,4} \equiv f'(p_{2,4})$ are the distribution functions of electrons and neutrons, $g_{2,4} \equiv g(p_{2,4})$ is the distribution function of ions, $\mathcal{M}_{12 \rightarrow 34}^{ei}$ and $\mathcal{M}_{12 \rightarrow 34}^{en}$ are the electron-ion and electron-neutron scattering matrix elements, respectively, and $\sum_i \equiv \int d\mathbf{p}_i / (2\pi)^3$. We will neglect the

electron-electron collision in this work as their rate is suppressed by a factor of Z^{-1} as compared to the rate of electron-ion scattering. As ions form a classical fluid in equilibrium, the function $g(p)$ is given by the Maxwell-Boltzmann distribution

$$g(p) = n_i \left(\frac{2\pi}{MT} \right)^{3/2} \exp \left(-\frac{p^2}{2MT} \right). \quad (6)$$

Additionally, we assume that the neutrons remain in thermal equilibrium and are therefore described by the Fermi-Dirac distribution

$$f(\epsilon) = \frac{1}{e^{\beta(\epsilon - \mu_n)} + 1}, \quad \epsilon = \frac{p^2}{2m_n^*}, \quad (7)$$

where m_n^* and μ_n are the effective neutron mass and chemical potential, respectively. In principle, the neutron effective mass should be computed self-consistently within the microscopic model that determines the composition of matter. However, its value is expected to deviate only weakly from the vacuum mass, and in what follows we therefore take $m_n^* \simeq m_n$.

To linearize the kinetic equation (3), the electron distribution is written as

$$f = f^0 + \delta f, \quad \delta f = -\phi \frac{\partial f^0}{\partial \epsilon}, \quad (8)$$

where $f^0(\epsilon)$ is the equilibrium Fermi-Dirac distribution function of electrons and $\delta f \ll f^0$ is a small perturbation. To derive the thermal conductivity under stationary conditions, we assume that the temperature $T = \beta^{-1}$ and the electron chemical potential μ vary slowly in space, i.e., $T = T(\mathbf{r})$, $\mu = \mu(\mathbf{r})$ and are independent of time. The leading-order non-vanishing derivatives appearing in the Boltzmann equation (3) then can be written as

$$\begin{aligned} \frac{\partial f^0}{\partial \mathbf{r}} &= \frac{\partial f^0}{\partial T} \frac{\partial T}{\partial \mathbf{r}} + \frac{\partial f^0}{\partial \mu} \frac{\partial \mu}{\partial \mathbf{r}} \\ &= \frac{\partial f^0}{\partial \epsilon} \left(\frac{\mu - \epsilon}{T} \nabla T - \nabla \mu \right), \end{aligned} \quad (9)$$

$$\frac{\partial f^0}{\partial \mathbf{p}} = \mathbf{v} \frac{\partial f^0}{\partial \epsilon}, \quad \frac{\partial f^0}{\partial \epsilon} = -\beta f^0(1 - f^0). \quad (10)$$

Note that in all terms involving spatial derivatives or the electric field, one may substitute $\mathbf{f} \rightarrow \mathbf{f}^0$. However, in the magnetic term, the perturbation must be retained, since in equilibrium the magnetic-field contribution vanishes due to $[\mathbf{v} \times \mathbf{B}](\partial f^0 / \partial \mathbf{p}) \propto [\mathbf{v} \times \mathbf{B}]\mathbf{v} = 0$. Therefore, for the third term in Eq. (3) we obtain [using Eqs. (8) and (10)]

$$e(\mathbf{E} + \mathbf{v} \times \mathbf{B}) \frac{\partial \mathbf{f}}{\partial \mathbf{p}} = e\mathbf{v} \cdot \mathbf{E} \frac{\partial f^0}{\partial \epsilon} - e[\mathbf{v} \times \mathbf{B}] \frac{\partial f^0}{\partial \epsilon} \frac{\partial \phi}{\partial \mathbf{p}}. \quad (11)$$

Substituting Eqs. (9)–(11) in Eq. (3), at linear order in macroscopic gradients, we find

$$\frac{\partial f^0}{\partial \epsilon} \left(e\mathbf{v} \cdot \mathbf{F} - e[\mathbf{v} \times \mathbf{B}] \frac{\partial \phi}{\partial \mathbf{p}} \right) = -I[\phi], \quad (12)$$

where we defined

$$\mathbf{F} = \mathbf{E}' + \frac{\epsilon - \mu}{eT} \nabla T, \quad e\mathbf{E}' = e\mathbf{E} + \nabla \mu. \quad (13)$$

Linearized collision integrals are given by

$$I_{ei}[\phi] = -(2\pi)^4 \beta \sum_{234} |\mathcal{M}_{12 \rightarrow 34}^{ei}|^2 \delta^{(4)}(p_1 + p_2 - p_3 - p_4) f_1^0 (1 - f_3^0) g_2(\phi_1 - \phi_3), \quad (14)$$

$$I_{en}[\phi] = -(2\pi)^4 \beta \sum_{234} |\mathcal{M}_{12 \rightarrow 34}^{en}|^2 \delta^{(4)}(p_1 + p_2 - p_3 - p_4) f_1^0 (1 - f_3^0) f_2'(1 - f_4')(\phi_1 - \phi_3), \quad (15)$$

where, as usual, we used the fact that the collision integral vanishes in equilibrium, since the corresponding combinations of distribution functions vanish. We search the solution of Eq. (12) in the form

$$\phi = \mathbf{p} \cdot \mathbf{A}(\epsilon), \quad (16)$$

where the vector \mathbf{A} depends only on the absolute value of \mathbf{p} . From Eqs. (12)–(16) we have

$$e\mathbf{v} \frac{\partial f^0}{\partial \epsilon} (\mathbf{F} + [\mathbf{A} \times \mathbf{B}]) = -I_{ei} - I_{en}, \quad (17)$$

with

$$I_{ei} = -(2\pi)^4 \beta \sum_{234} |\mathcal{M}_{12 \rightarrow 34}^{ei}|^2 \delta^{(4)}(p_1 + p_2 - p_3 - p_4) \times f_1^0 (1 - f_3^0) g_2(\mathbf{p}_1 \cdot \mathbf{A}_1 - \mathbf{p}_3 \cdot \mathbf{A}_3), \quad (18)$$

$$I_{en} = -(2\pi)^4 \beta \sum_{234} |\mathcal{M}_{12 \rightarrow 34}^{en}|^2 \delta^{(4)}(p_1 + p_2 - p_3 - p_4) \times f_1^0 (1 - f_3^0) f_2'(1 - f_4')(\mathbf{p}_1 \cdot \mathbf{A}_1 - \mathbf{p}_3 \cdot \mathbf{A}_3). \quad (19)$$

Since the energy transfer in collisions with both nuclei and neutrons is small, we approximate $\mathbf{A}_1 \approx \mathbf{A}_3$ in Eqs. (18) and (19), allowing \mathbf{A}_1 to be taken outside the

collision integrals ($\mathbf{p}_1 \equiv \mathbf{p}$)

$$\begin{aligned} I_{ei} &= -(2\pi)^4 \beta \sum_{234} |\mathcal{M}_{12 \rightarrow 34}^{ei}|^2 \delta^{(4)}(p_1 + p_2 - p_3 - p_4) \\ &\times f_1^0 (1 - f_3^0) g_2[\mathbf{A} \cdot (\mathbf{p}_1 - \mathbf{p}_3)] = \frac{\partial f^0}{\partial \epsilon} (\mathbf{A} \cdot \mathbf{p}) \tau_{ei}^{-1}(\epsilon), \quad (20) \\ I_{en} &= -(2\pi)^4 \beta \sum_{234} |\mathcal{M}_{12 \rightarrow 34}^{en}|^2 \delta^{(4)}(p_1 + p_2 - p_3 - p_4) \\ &\times f_1^0 (1 - f_3^0) f_2'(1 - f_4')[\mathbf{A} \cdot (\mathbf{p}_1 - \mathbf{p}_3)] = \frac{\partial f^0}{\partial \epsilon} (\mathbf{A} \cdot \mathbf{p}) \tau_{en}^{-1}(\epsilon), \quad (21) \end{aligned}$$

where $\mathbf{q} = \mathbf{p}_1 - \mathbf{p}_3 = \mathbf{p}_4 - \mathbf{p}_2$ is the transferred momentum, and we defined electron-ion and electron-neutron collision rates, *i.e.*, inverse relaxation times by ($\epsilon \equiv \epsilon_1$)

$$\tau_{ei}^{-1}(\epsilon) = (2\pi)^{-5} \int d\mathbf{q} \int d\mathbf{p}_2 |\mathcal{M}_{12 \rightarrow 34}^{ei}|^2 \frac{\mathbf{q} \cdot \mathbf{p}}{p^2} \delta(\epsilon + \epsilon_2 - \epsilon_3 - \epsilon_4) \frac{1 - f_3^0}{1 - f_1^0} g_2, \quad (22)$$

$$\tau_{en}^{-1}(\epsilon) = (2\pi)^{-5} \int d\mathbf{q} \int d\mathbf{p}_2 |\mathcal{M}_{12 \rightarrow 34}^{en}|^2 \frac{\mathbf{q} \cdot \mathbf{p}}{p^2} \delta(\epsilon + \epsilon_2 - \epsilon_3 - \epsilon_4) \frac{1 - f_3^0}{1 - f_1^0} f_2'(1 - f_4'). \quad (23)$$

Substituting the collision integrals given by Eqs. (20) and (21) into Eq. (17) we obtain

$$e\tau\epsilon^{-1}\mathbf{F} + \omega_c\tau[\mathbf{A} \times \mathbf{b}] + \mathbf{A} = 0, \quad (24)$$

where

$$\tau^{-1} = \tau_{en}^{-1} + \tau_{ei}^{-1} \quad (25)$$

is the effective electron relaxation rate, $\omega_c = eB\epsilon^{-1}$ is the cyclotron frequency, and $\mathbf{b} = \mathbf{B}/B$ is the unit vector along the magnetic field. We search the vector \mathbf{A} in the form $\mathbf{A} = \alpha\mathbf{f} + \beta(\mathbf{f} \cdot \mathbf{b})\mathbf{b} + \gamma[\mathbf{f} \times \mathbf{b}]$, with unit vector $\mathbf{f} = \mathbf{F}/F$ and energy-dependent coefficients α, β, γ . Substituting this expression into Eq. (24) and equating the coefficients of the three independent vectors \mathbf{f}, \mathbf{b} and $[\mathbf{f} \times \mathbf{b}]$, we obtain

$$\phi = -\frac{e\tau}{1 + (\omega_c\tau)^2} v_i [\delta_{ij} - \omega_c\tau\epsilon_{ijk}b_k + (\omega_c\tau)^2 b_i b_j] F_j. \quad (26)$$

The electron-ion and electron-neutron scattering matrix elements can be evaluated using standard QED techniques for thermal media. The electron-ion scattering amplitude incorporates ion-ion correlations through the structure factor $S(q)$ of a one-component plasma, as well as Debye screening via the low-frequency limit of the HTL polarization tensor of a QED plasma (see Sec. IV of Ref. [18] for details). Since nuclei in the inner crust have relatively large radii, finite-size effects must also be included through the nuclear form factor $F(q)$, given by [39]

$$F(q) = -3 \frac{qr_c \cos(qr_c) - \sin(qr_c)}{(qr_c)^3}. \quad (27)$$

The final expression for the electron-ion relaxation is given by [18]

$$\tau_{ei}^{-1}(\epsilon) = \frac{\pi Z^2 \alpha^2 n_i}{\epsilon p^3} \int_0^{2p} dq q^3 S(q) F^2(q) \frac{4\epsilon^2 - q^2}{|q^2 + q_D^2|^2}, \quad (28)$$

where $\alpha = 1/137$ is the fine-structure constant, and the Debye wave-number q_D is defined as

$$q_D^2 = -\frac{4\alpha}{\pi} \int_0^\infty dp p^2 \frac{\partial f^0}{\partial \epsilon}. \quad (29)$$

For numerical computations, we will use the structure factor of one-component plasma [5, 40, 41], previously employed in Refs. [17–19].

The scattering matrix for the electron scattering off the anomalous magnetic moment of neutrons at finite temperatures is computed in Appendix A, which is followed by the computation of the corresponding collision rate in Appendix B. We find that in the regime of interest $\tau_{en} \gg \tau_{ei}$, indicating that electron–neutron scattering has a negligible effect on electron transport in the liquid phase in the inner crust across the temperatures considered. The minor role of electron–neutron scattering in the inner crust was also noted earlier in Ref. [1], which focused on low-temperature crystallized matter, a conclusion that is also valid if the induced interaction between electrons and neutrons is taken into account [22].

B. Thermoelectric currents and transport coefficients

Now we are in a position to calculate the electrical and thermal currents using the solution (8), (26) and the expression (13) for \mathbf{F}

$$j_k = - \int \frac{2d\mathbf{p}}{(2\pi)^3} e v_k \delta f = \sigma_{kj} E'_j - \alpha_{kj} \partial_j T, \quad (30)$$

$$q_k = \int \frac{2d\mathbf{p}}{(2\pi)^3} (\epsilon - \mu) v_k \delta f = \tilde{\alpha}_{kj} E'_j - \tilde{\kappa}_{kj} \partial_j T, \quad (31)$$

where the transport coefficient tensors are defined as

$$\sigma_{kj} = - \int \frac{2d\mathbf{p}}{(2\pi)^3} \frac{\partial f^0}{\partial \epsilon} \frac{e^2 \tau}{1 + (\omega_c \tau)^2} v_k v_i \times [\delta_{ij} - \omega_c \tau \epsilon_{ijm} b_m + (\omega_c \tau)^2 b_i b_j], \quad (32)$$

$$\alpha_{kj} = \int \frac{2d\mathbf{p}}{(2\pi)^3} \frac{\partial f^0}{\partial \epsilon} \frac{e(\epsilon - \mu) \tau}{1 + (\omega_c \tau)^2} v_k v_i \times [\delta_{ij} - \omega_c \tau \epsilon_{ijm} b_m + (\omega_c \tau)^2 b_i b_j] T^{-1}, \quad (33)$$

$$\tilde{\alpha}_{kj} = \int \frac{2d\mathbf{p}}{(2\pi)^3} \frac{\partial f^0}{\partial \epsilon} \frac{e(\epsilon - \mu) \tau}{1 + (\omega_c \tau)^2} v_k v_i \times [\delta_{ij} - \omega_c \tau \epsilon_{ijm} b_m + (\omega_c \tau)^2 b_i b_j], \quad (34)$$

$$\tilde{\kappa}_{kj} = - \int \frac{2d\mathbf{p}}{(2\pi)^3} \frac{\partial f^0}{\partial \epsilon} \frac{(\epsilon - \mu)^2 \tau}{1 + (\omega_c \tau)^2} v_k v_i \times [\delta_{ij} - \omega_c \tau \epsilon_{ijm} b_m + (\omega_c \tau)^2 b_i b_j] T^{-1}. \quad (35)$$

Equations (30) and (31) can equivalently be written as

$$\mathbf{E}' = \hat{\rho} \mathbf{j} - \hat{Q} \nabla T, \quad \mathbf{q} = -\hat{\kappa} \nabla T - T \hat{Q} \mathbf{j}, \quad (36)$$

where $\hat{\sigma}$ and $\hat{\rho} = \hat{\sigma}^{-1}$ are the conductivity and resistivity tensors, respectively; $\hat{Q} = -\hat{\rho} \hat{\alpha}$ is the thermopower and $\hat{\kappa} = \hat{\tilde{\kappa}} + T \hat{\alpha} \hat{Q}$ is the thermal conductivity. The tensors $\hat{\sigma}$, $\hat{\alpha}$, $\hat{\tilde{\kappa}}$ and $\hat{\tilde{\kappa}}$ are given by

$$\hat{\sigma} = e^2 \hat{\mathcal{L}}^0, \quad \hat{\alpha} = T \hat{\alpha} = -e T \hat{\mathcal{L}}^1, \quad \hat{\kappa} = T \hat{\mathcal{L}}^2, \quad (37)$$

with

$$\mathcal{L}_{kj}^n = \delta_{kj} \mathcal{L}_0^n - \epsilon_{kjm} b_m \mathcal{L}_1^n + b_k b_j \mathcal{L}_2^n, \quad (38)$$

$$\mathcal{L}_l^n = -\frac{1}{3\pi^2} \int_{m_e}^\infty d\epsilon \frac{\partial f^0}{\partial \epsilon} \left(\frac{\epsilon - \mu}{T} \right)^n \mathcal{F}_l(\epsilon),$$

$$\mathcal{F}_l(\epsilon) = \frac{p^3}{\epsilon} \frac{\tau (\omega_c \tau)^l}{1 + (\omega_c \tau)^2}, \quad l = 0, 1, 2. \quad (39)$$

In the absence of a magnetic field $\hat{\mathcal{L}}^n$ tensors become diagonal $\mathcal{L}_{kj}^n = \delta_{kj} \mathcal{L}^n$ with

$$\mathcal{L}^n = -\frac{1}{3\pi^2} \int_{m_e}^\infty d\epsilon \frac{p^3}{\epsilon} \frac{\partial f^0}{\partial \epsilon} \left(\frac{\epsilon - \mu}{T} \right)^n \tau = \mathcal{L}_0^n + \mathcal{L}_2^n. \quad (40)$$

With the magnetic field along z axis, we have

$$\hat{\mathcal{L}}^n = \begin{pmatrix} \mathcal{L}_0^n & -\mathcal{L}_1^n & 0 \\ \mathcal{L}_1^n & \mathcal{L}_0^n & 0 \\ 0 & 0 & \mathcal{L}^n \end{pmatrix}, \quad (41)$$

where \mathcal{L}^n , \mathcal{L}_0^n and \mathcal{L}_1^n are, respectively, the longitudinal, transverse, and Hall components of this tensor. A similar tensor structure applies to all transport coefficients defined above. Using Eqs. (37)–(41), it is straightforward to obtain the components of thermopower

$$Q = -\frac{\alpha}{\sigma}, \quad Q_0 = -\frac{\alpha_0 \sigma_0 + \alpha_1 \sigma_1}{\sigma_0^2 + \sigma_1^2}, \quad Q_1 = -\frac{\alpha_1 \sigma_0 - \alpha_0 \sigma_1}{\sigma_0^2 + \sigma_1^2}, \quad (42)$$

and thermal conductivity

$$\kappa = \tilde{\kappa} + T \alpha Q = \tilde{\kappa} - T \frac{\alpha^2}{\sigma}, \quad (43)$$

$$\kappa_0 = \tilde{\kappa}_0 + T(\alpha_0 Q_0 - \alpha_1 Q_1), \quad (44)$$

$$\kappa_1 = \tilde{\kappa}_1 + T(\alpha_0 Q_1 + \alpha_1 Q_0). \quad (45)$$

Thus, the components of conductivities and thermopower are fully determined if the relaxation time τ is known. The low-temperature expressions of the transport coefficients are derived in Appendix C.

IV. NUMERICAL RESULTS

Numerically, the thermal conductivity and thermopower are evaluated using the relaxation time given

by Eq. (28) and the formulas (37), (42)–(45). We recall that for large magnetic fields ($\omega_c \tau \gtrsim 1$) the full tensor structure of these coefficients must be taken into account, while for weak magnetic fields ($\omega_c \tau \ll 1$) only the longitudinal components κ and Q are relevant. Below, we will study the dependence of these transport coefficients on density, temperature, and magnetic field strength for the selected compositions. The numerical results will be presented in c.g.s. units, which are common in astrophysical applications.

A. Relaxation time and Hall parameter

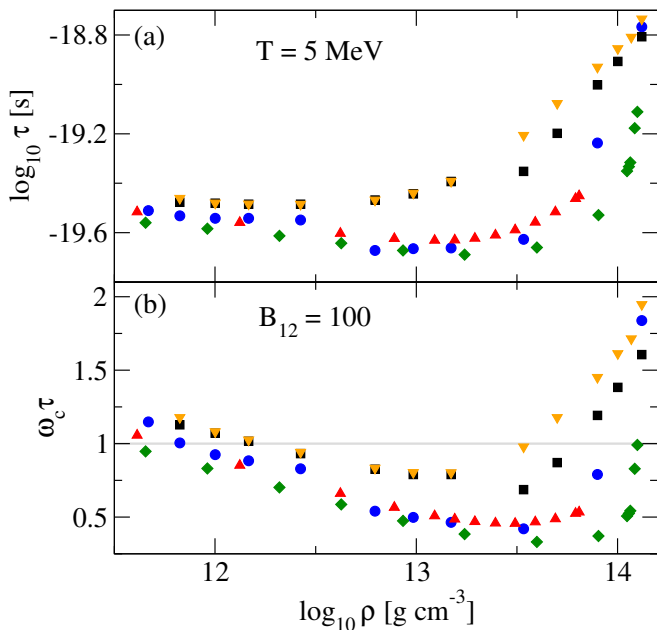


FIG. 2: (a) The relaxation time τ and (b) the Hall parameter $\omega_c \tau$ as functions of density for five compositions as labeled in Fig. 1. The temperature is fixed at $T = 5$ MeV, and the magnetic field is fixed at $B_{12} = 100$.

The behavior of the relaxation time, τ , and the Hall parameter, $\omega_c \tau$, was discussed in detail in Ref. [17] in the context of electrical conductivity; here, we summarize the most important features. Figure 2 shows the density dependence of the relaxation time and the Hall parameter at the Fermi energy for five different compositions at $T = 5$ MeV. The variations in τ and $\omega_c \tau$ among the compositions are primarily due to differences in nuclear size, which affect the nuclear form factor, $F(q)$, particularly at high densities, $\log_{10} \rho [\text{g cm}^{-3}] > 13$.

The finite nuclear size leads to an increase in the relaxation time with density, due to the suppression of electron-ion scattering rates compared to scattering off a point-like nucleus. This effect is particularly significant for the D1M and D1M* models, which have larger nuclei in the high-density regime, as seen in Fig. 1. Figure 3

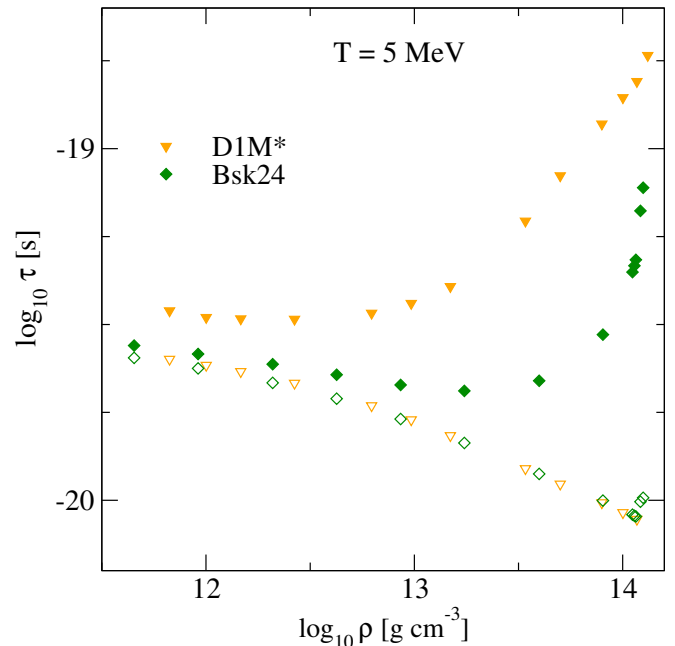


FIG. 3: Density-dependence of the relaxation time for two models evaluated with full nuclear formfactor $F(q)$ (filled symbols) and with $F(q) = 1$ (empty symbols). The temperature is fixed at $T = 5$ MeV.

shows the relaxation time for the D1M* and Bsk24 models, which predict very similar values of Z and R_{WS} , but rather different values of A and r_c . Consequently, the effect of the nuclear form factor is markedly different for these two models. Indeed, as seen in the figure, the relaxation times for both models would be nearly identical if the effect of $F(q)$ were neglected, i.e., $F(q) \rightarrow 0$ (empty symbols).

Panel (b) of Fig. 2 shows the Hall parameter for a magnetic field $B_{12} \equiv B/(10^{12} \text{ G}) = 100$. At this field strength, $\omega_c \tau$ is of order unity throughout the inner crust. Consequently, the inner crust becomes anisotropic at such field strengths, although the effect is already negligible for $B_{12} \lesssim 13$. We also note that the anisotropy is more pronounced at higher densities for models with larger nuclei, where the nuclear form factor plays a dominant role.

B. Longitudinal thermal conductivity

We start with the results concerning the density dependence of the scalar thermal conductivity, κ , at a fixed temperature. Figure 4 shows κ as a function of density for $T = 5$ MeV. Despite the non-monotonic behavior of the relaxation time with density, the increasing density of states near the Fermi surface leads to a growth of the thermal conductivity with matter density, as also suggested by the low-temperature formula (C9) for κ . Since

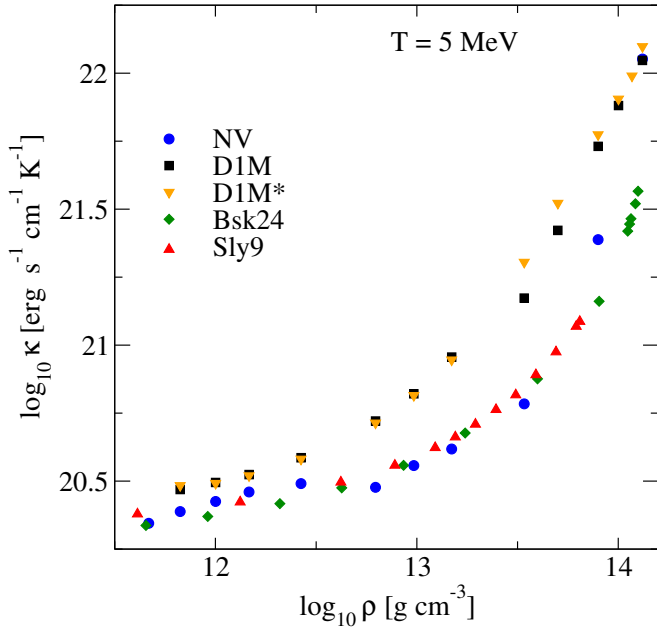


FIG. 4: Dependence of the scalar conductivity on density for five compositions. The temperature is fixed at $T = 5$ MeV.

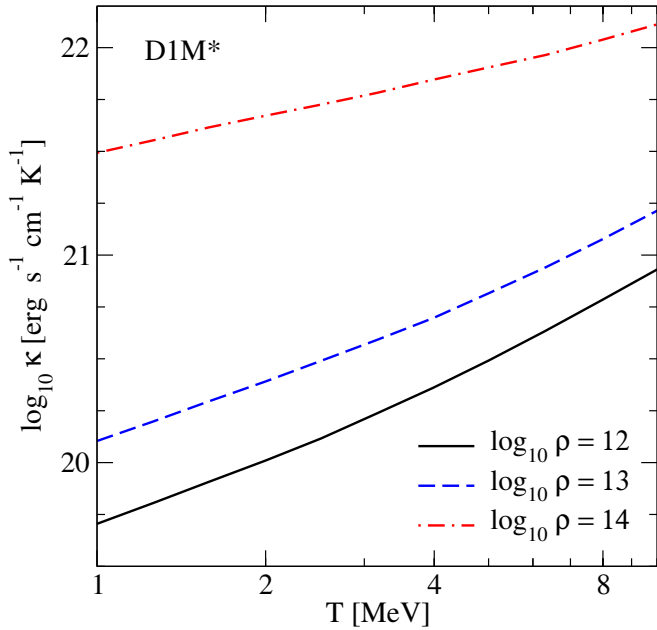


FIG. 5: The temperature dependence of the scalar conductivity for various values of the density for composition D1M*.

Z varies little across the inner crust, remaining fixed at a (semi)magic number—the density dependence of κ is governed primarily by the variation of A , which influences the thermal conductivity through the nuclear form factor. As shown in Fig. 4, the discrepancies among different compositions grow with increasing density, reaching factors 3-4 of $\log_{10} \rho \geq 13$.

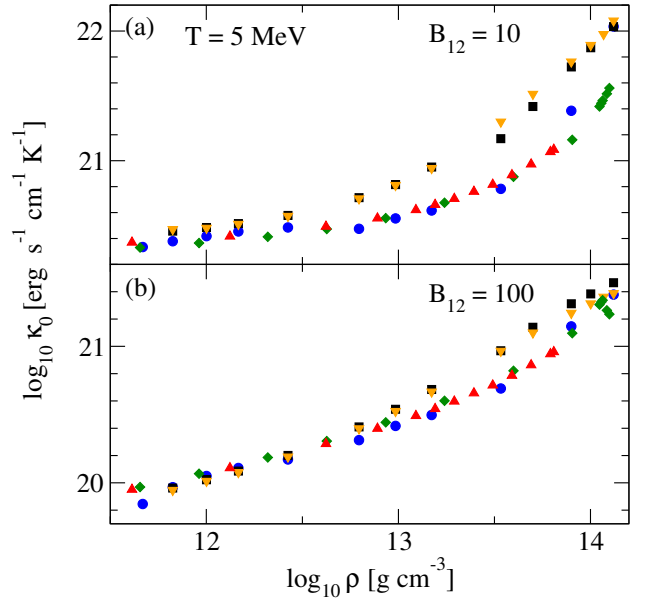


FIG. 6: The same as in Fig. 4 but for κ_0 and for two magnetic fields $B_{12} = 10$ and $B_{12} = 11$.

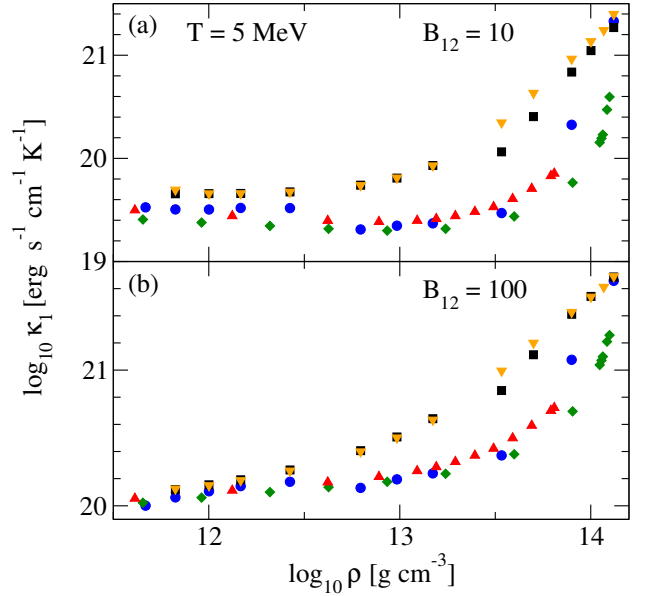


FIG. 7: The same as in Fig. 4 but for κ_1 and for two magnetic fields $B_{12} = 10$ and $B_{12} = 11$.

The temperature dependence of the thermal conductivity for the D1M* model at fixed densities is shown in Fig. 5. In the range $0 \leq T \leq 10$ MeV, the thermal conductivity increases with temperature, consistent with the low- T asymptotic formula (C9). At low densities, where the relaxation time depends weakly on temperature, κ increases almost linearly with T . In the high-density regime, where the effect of the form factor is more pronounced, we find approximate scaling $\kappa \propto T^{0.5}$. We

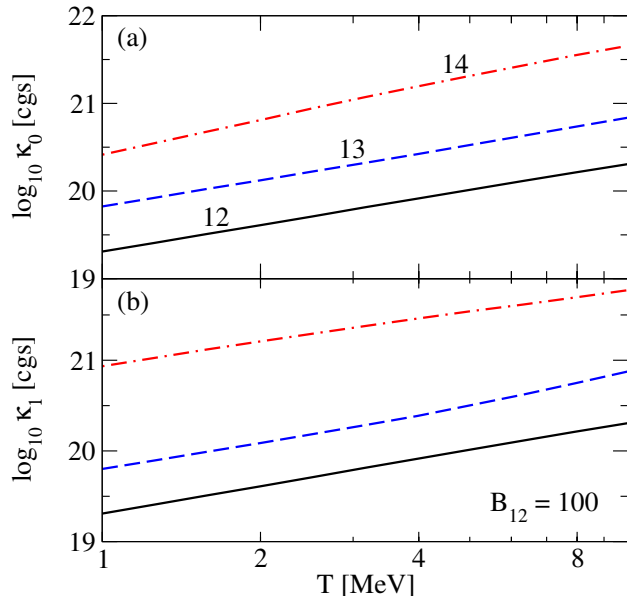


FIG. 8: Temperature dependence of κ_0 and κ_1 at fixed magnetic field value $B_{12} = 100$. Curves correspond to several fixed densities, distinguished in the plot by the logarithm of their values, for the D1M* composition.

note that the asymptotic formula (C9) is not exact at $T \simeq 10$ MeV and moderate densities $\log_{10} \rho \leq 13$, where electrons are semi-degenerate. In this case, κ grows faster than linearly due to the additional increase in electron energy, which expands the phase space for thermal conduction.

C. Transverse and Hall conductivities

Now we consider strong magnetic fields, where the transverse and Hall components of the thermal conductivity become relevant. Figure 6 shows the density dependence of the κ_0 component for two values of the magnetic field ($B_{12} = 10, 100$) for selected compositions at $T = 5$ MeV. Figure 7 presents the same for the κ_1 component.

For $B_{12} = 10$, we have $\omega_c \tau \ll 1$, corresponding to essentially isotropic conduction. In this case, κ_0 is almost identical to the scalar conductivity κ , as seen by comparing Figs. 4 and 6, while κ_1 remains much smaller. For $B_{12} = 100$, anisotropy is already significant, as also indicated by Fig. 2. Here, the transverse and Hall conductivities, κ_0 and κ_1 , are of comparable magnitude.

The temperature dependence of κ_0 and κ_1 for the D1M* model is shown in Fig. 8, with $B_{12} = 100$ – a value of the B -field for which $\omega_c \tau \sim 1$. Both components grow nearly linearly with temperature, as implied by Eq. (C9), since the numerators and denominators in the fractions containing τ effectively cancel.

Figure 9 shows the magnetic field dependence of these

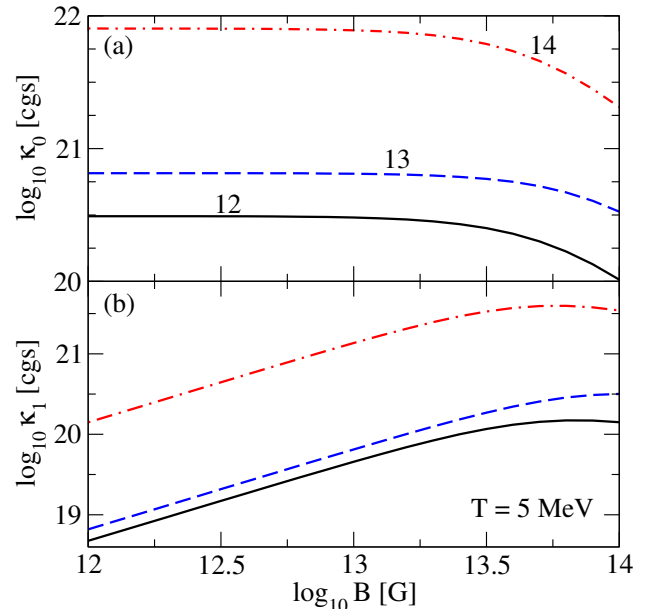


FIG. 9: Magnetic field dependence of κ_0 and κ_1 at fixed temperature $T = 5$ MeV. Curves correspond to several fixed densities, distinguished in the plot by the logarithm of their values, for the D1M* composition.

components at fixed temperature and density. According to Eq. (C17), in the low-field regime κ_1 is proportional to the magnetic field, whereas κ_0 is essentially independent of it; these trends are visible in Fig. 9. Anisotropy becomes important for $B_{12} \gtrsim 30$, where κ_0 begins to decrease, and κ_1 approaches its maximum. Overall, the effect of the magnetic field on thermal conductivity in the inner crust up to $B_{12} \simeq 100$ is less pronounced than in the outer crust, which becomes fully anisotropic for $B_{12} \gtrsim 10$ [18, 19].

D. Thermopower

The dependence of the longitudinal thermopower, Q , on density and temperature is shown in Figs. 10 and 11, respectively. In essence, Q is a thermodynamic quantity and is practically independent of the microscopic relaxation time. Indeed, the τ -dependence in Q arises from both α and σ , which almost entirely cancel each other, as seen from Eq. (42). Consequently, the behavior of Q differs quantitatively from that of the conductivities. In contrast to the thermal conductivity, the thermopower decreases with density. This reversed density dependence is evident from the low-temperature formula (C14), which implies the scaling $Q \propto T n_i^{-1/3}$. This scaling also explains the weak composition dependence of Q up to the highest densities in the crust, clearly seen in Fig. 10. As a function of temperature, thermopower exhibits an almost linear scaling, consistent with the low- T asymptotics, as

shown in Fig. 11.

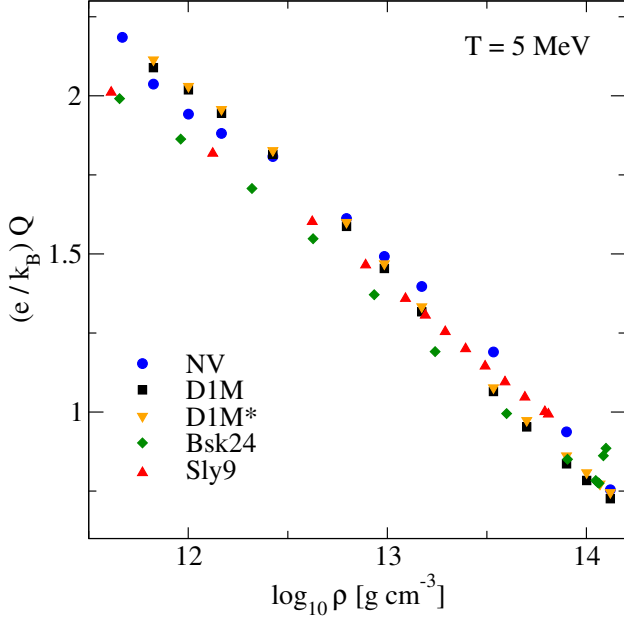


FIG. 10: Dependence of thermopower Q on density for five compositions. The temperature is fixed at $T = 5$ MeV.

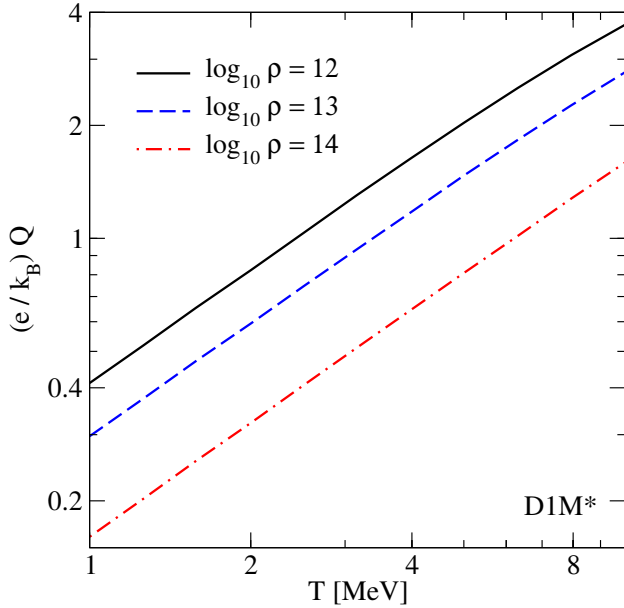


FIG. 11: Dependence of thermopower Q on temperature for various densities, as indicated in the plot, for the D1M* composition.

The transverse component, Q_0 , does not differ significantly from the longitudinal component Q , as implied by the limiting formula (C14). Its density and temperature dependence is nearly identical to that of Q , and its magnetic field dependence is very weak throughout

the regime of interest (Figs. 12, 14, and 15). Specifically, Eq. (C14) gives $Q_0 \rightarrow Q$ for $\omega_c \tau \ll 1$, while the lowest value, $Q_0 \rightarrow 3Q/4$, occurs for $\omega_c \tau \gg 1$.

The Hall component of thermopower, Q_1 , is shown as a function of density in Fig. 13. As seen, Q_1 differs significantly among compositions: D1M and D1M* predict higher values, Bsk24 and Sly9 predict smaller values, and NV is intermediate. This scatter reflects the nontrivial dependence of Q_1 on the relaxation timescale, which does not cancel in contrast to Q_0 , as seen from Eq. (C14).

The temperature dependence of Q_1 at fixed densities and magnetic field is shown in Fig. 14. Although Q_1 increases with temperature more rapidly than Q_0 , it remains smaller in magnitude. Figure 15 presents the magnetic-field dependence of Q_1 for three representative densities at fixed temperature. The behavior of Q_1 closely mirrors that of κ_1 : it grows with increasing field strength up to $B_{12} \simeq 30$, where it reaches a maximum.

E. Magnetic field evolution timescales

We now provide simple estimates for the characteristic timescales of magnetic field evolution using our numerical results for thermopower and the electrical conductivity results from Ref. [17]. The evolution of low-frequency magnetic fields in neutron stars is governed by Maxwell's equations:

$$\nabla \times \mathbf{E} = -\frac{\partial \mathbf{B}}{\partial t}, \quad \nabla \times \mathbf{B} = 4\pi \mathbf{j}, \quad (46)$$

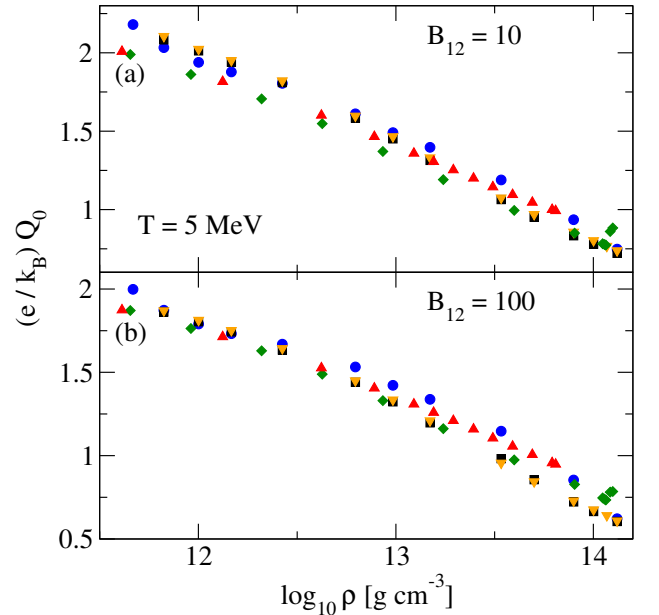


FIG. 12: Dependence of the Q_0 component of thermopower on density for five compositions. The values of the temperature and the magnetic field are indicated in the plot.

where we assume the magnetic permeability of matter is unity and neglect the displacement current. Substituting the electric field from Eq. (36), $\mathbf{E} = \hat{\rho}\mathbf{j} - \hat{Q}\nabla T - \nabla\mu/e$, we obtain the induction equation including thermoelectric effects:

$$\begin{aligned}\frac{\partial \mathbf{B}}{\partial t} &= -\nabla \times \left(\hat{\rho}\mathbf{j} - \hat{Q}\nabla T - \frac{1}{e}\nabla\mu \right) \\ &= -\frac{1}{4\pi}\nabla \times (\hat{\rho}\nabla \times \mathbf{B}) + \nabla \times (\hat{Q}\nabla T),\end{aligned}\quad (47)$$

where we used $\nabla \times \nabla\mu = 0$. For moderate fields, $B_{12} \leq 10$, Eq. (47) can be taken in the isotropic approximation:

$$\frac{\partial \mathbf{B}}{\partial t} = -\frac{1}{4\pi}\nabla \times \left(\frac{\nabla \times \mathbf{B}}{\sigma} \right) + \nabla \times (Q\nabla T). \quad (48)$$

Assuming that the characteristic length scale over which the magnetic field varies, L_B , is smaller than the scale of variation of density and temperature, L , we can treat σ as constant over L_B . Using $\nabla \times (\nabla \times \mathbf{B}) = \nabla(\nabla \cdot \mathbf{B}) - \Delta \mathbf{B}$ and $\nabla \cdot \mathbf{B} = 0$, we obtain:

$$\frac{\partial \mathbf{B}}{\partial t} = \frac{1}{4\pi\sigma}\Delta \mathbf{B} + \nabla Q \times \nabla T. \quad (49)$$

A simple estimate of the magnetic field evolution timescale, τ_B , follows from approximating $|\partial \mathbf{B}/\partial t| \simeq B/\tau_B$, $|\Delta \mathbf{B}| \simeq B/L_B^2$, $|\nabla Q| \simeq Q/L$, and $|\nabla T| \simeq T/L$:

$$\frac{B}{\tau_B} = \left| \frac{B}{4\pi\sigma L_B^2} \pm \frac{QT}{L^2} \right|. \quad (50)$$

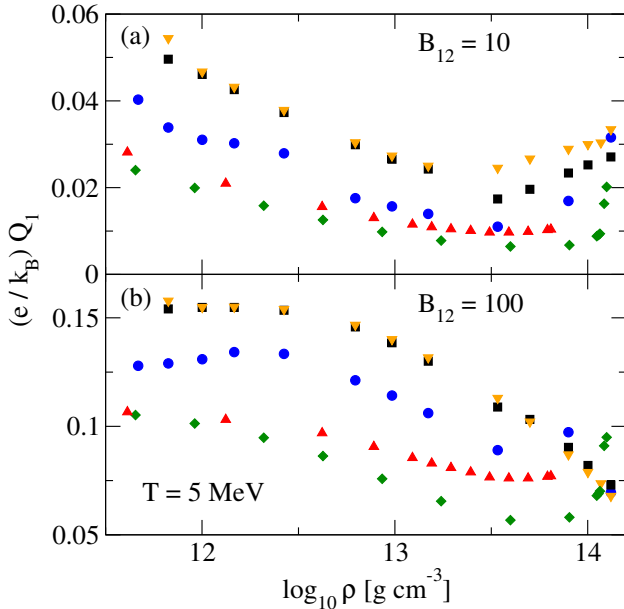


FIG. 13: Dependence of the Hall thermopower Q_1 on density for five compositions. The values of the temperature and the magnetic field are indicated in the plot.

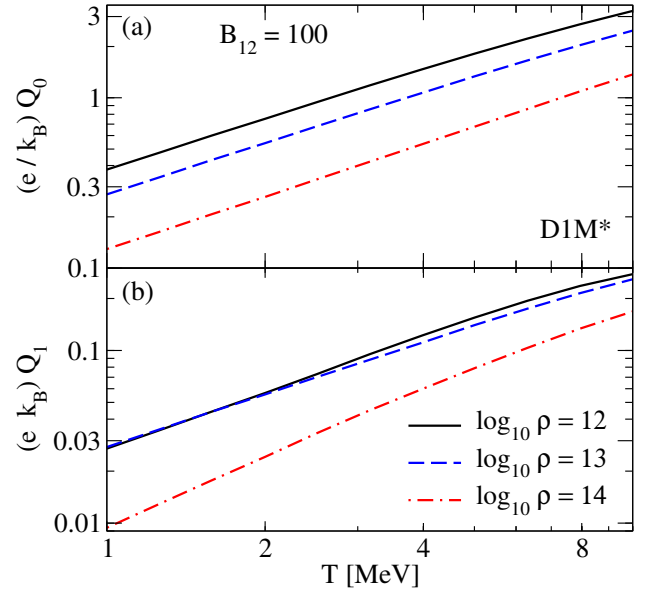


FIG. 14: Dependence of Q_0 and Q_1 components of thermopower on temperature for various values of density for model D1M*.

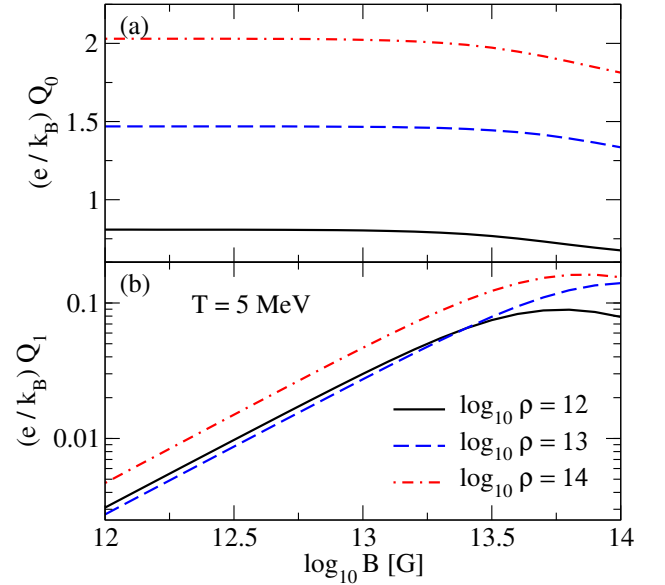


FIG. 15: Dependence of Q_0 and Q_1 components of thermopower on the magnetic field for various values of the density for D1M*.

Thus, the magnetic field decay timescale, which includes thermoelectric effects is given by

$$\tau_B^{-1} = |\tau_\sigma^{-1} \pm \tau_Q^{-1}|, \quad \tau_\sigma = 4\pi\sigma L_B^2, \quad \tau_Q = \frac{BL^2}{QT}, \quad (51)$$

where τ_σ corresponds to Ohmic dissipation and τ_Q is a timescale associated with thermoelectric effects. The evolution of the neutron star crustal field is governed by

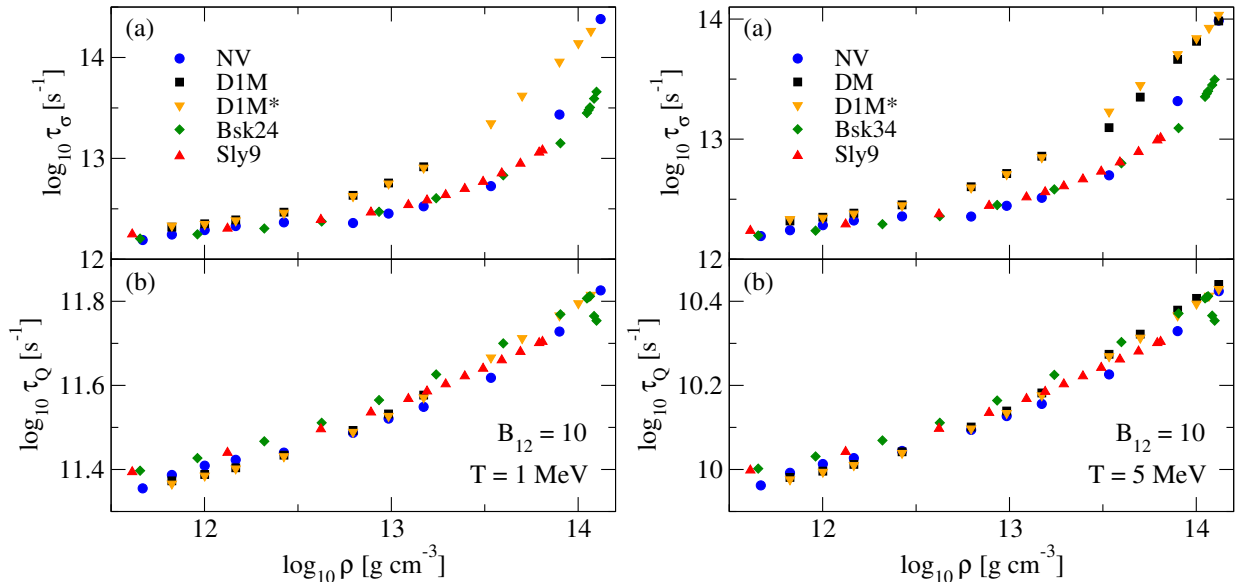


FIG. 16: Magnetic field decay time scales due to the Ohmic dissipation τ_σ [panels (a)] and thermoelectric effects τ_Q [panels (b)] as functions of density for five compositions. The temperature is fixed at $T = 1$ MeV in the left figure and $T = 5$ MeV in the right figure.

the smaller of these two. Figure 16 shows these timescales as functions of density for $B_{12} = 10$ and temperatures $T = 1$ MeV and $T = 5$ MeV, with $L = 10$ km and $L_B = 1$ km, relevant for post-merger matter [20].

The Ohmic timescale τ_σ is independent of B and nearly independent of T , whereas τ_Q is proportional to B and inversely proportional to T^2 . We find that τ_Q is always at least by an order of magnitude smaller across the studied densities and temperatures, as long as isotropic conduction is a good approximation. For more homogeneous magnetic fields, thermoelectric effects become even more significant due to their dependence on L and L_B .

We conclude that thermoelectric effects can play a significant role in the magnetic-field evolution of a moderately magnetized neutron star inner crust at sufficiently high temperatures, $T \gtrsim 1$ MeV. For stronger magnetic fields, such as those typical of magnetars, the temperature range in which thermoelectricity influences the crustal field evolution becomes correspondingly narrower as the temperature increases.

V. SUMMARY

In this work, we calculated the thermal conductivity and thermopower at densities corresponding to the inner crusts of neutron stars, in the regime where ions are in a liquid state. In this regime, electrons are the main carriers of charge and heat, and the dominant channel of dissipation is their scattering off correlated nuclei via screened electromagnetic interactions. The Boltzmann kinetic equation was solved in the relaxation time ap-

proximation in the simultaneous presence of electromagnetic fields and thermal gradients. We analyzed the general tensor structure of the transport coefficients, including the effects of ion-ion correlations and finite nuclear size. Additionally, we computed the exact rate of electron scattering on the anomalous magnetic moment of free neutrons at finite temperatures and found that its contribution to electron transport is strongly suppressed.

For numerical calculations, five different nuclear compositions of the inner crust were considered. The nuclear form factor was found to be the dominant factor governing both the magnitude of the thermal conductivity and its scatter among different compositions at high densities. Thermal conduction becomes anisotropic for magnetic fields $B_{12} \gtrsim 30$, with the transverse and Hall components suppressed relative to the longitudinal component. In contrast, thermopower exhibits more universal behavior, being largely independent of the relaxation time.

Using these results for conductivity and thermopower, we estimated the magnetic field evolution timescales in the neutron star inner crust, including thermoelectric effects. Our analysis shows that thermoelectricity can dominate the magnetic field evolution in a moderately heated and magnetized inner crust. At lower temperatures and/or higher magnetic fields, the role of pure thermal conductivity becomes increasingly important.

Acknowledgements

The authors acknowledge support from the collaborative research grant No. 24RL-1C010 provided by the Higher Education and Science Committee (HESC) of

the Republic of Armenia through the “Remote Laboratory” program. A. S. also acknowledges support from the Deutsche Forschungsgemeinschaft Grant No. SE 1836/6-1 and the Polish National Science Centre (NCN) Grant No. 2023/51/B/ST9/02798.

Appendix A: Electron-neutron scattering matrix element

In this Appendix, we compute the leading-order matrix element for electron–neutron scattering via virtual plasmon exchange, where the neutron couples to the plasmon only through its anomalous magnetic moment. The Lagrangian of this interaction is given by

$$\mathcal{L}_{\text{int}} = -\frac{e\kappa_n}{4m_n}\bar{\psi}_n\sigma^{\mu\nu}\psi_n F_{\mu\nu}, \quad \sigma^{\mu\nu} = \frac{i}{2}(\gamma^\mu\gamma^\nu - \gamma^\nu\gamma^\mu), \quad (\text{A1})$$

where $\kappa_n \approx -1.91$ is the neutron’s anomalous magnetic moment in nuclear magnetons, m_n is the neutron mass, and $F_{\mu\nu}$ is the electromagnetic field tensor. The effective vertex for the electron-neutron scattering can be read off from Eq. (A1)

$$\Gamma^\mu = i\frac{e\kappa_n}{2m_n}\sigma^{\mu\nu}q_\nu, \quad (\text{A2})$$

where q^ν is the plasmon momentum entering the vertex, *i.e.*, the momentum transfer in the scattering process. In a thermal medium, this process is mediated by screened interaction corresponding to a plasmon exchange, as illustrated in Fig. 17; (see Ref. [18] and references therein for more detailed discussion of HTL approximation.) We split the matrix element corresponding to this process into longitudinal and transverse parts

$$\mathcal{M}_{12\rightarrow 34}^{en} = \frac{ie^2\kappa_n}{2m_n}(\mathcal{M}_L - \mathcal{M}_T), \quad \mathcal{M}_L = \frac{J_e^0 J_n^0}{q^2 + \Pi_L}, \quad \mathcal{M}_T = \frac{J_{e\perp}^i J_{n\perp}^i}{q^2 - \omega^2 + \Pi_T}, \quad (\text{A3})$$

where we defined the electron and neutron 4-currents as

$$J_e^\mu = \bar{u}_e(k')\gamma^\mu u_e(k), \quad J_n^\nu = \bar{u}_n(p')(\sigma^{\nu\lambda}q_\lambda)u_n(p). \quad (\text{A4})$$

Here k, k' are the initial and final 4-momenta of the electron, p, p' are the initial and final 4-momenta of the neutron, $q = (\omega, \mathbf{q}) = k - k' = p' - p$, and $\mathbf{J}_{e\perp}, \mathbf{J}_{n\perp}$ are the components of these currents transverse to \mathbf{q} .

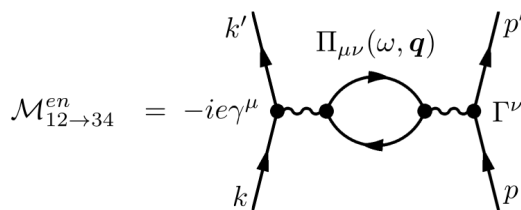


FIG. 17: Diagram describing the electron-neutron scattering via exchange of a virtual plasmon. The plasmon self-energy is given by the polarization tensor $\Pi_{\mu\nu}(\omega, \mathbf{q})$ shown by the closed loop.

The screening of the interaction is taken into account in terms of the longitudinal $\Pi_L(\omega, q)$ and transverse $\Pi_T(\omega, q)$ components of the plasmon polarization tensor. We will employ here the results of the HTL effective field theory calculations for ultrarelativistic electrons [18, 36, 37]

$$\Pi_L(\omega, q) = q_D^2 \left[1 - \frac{x}{2} \log \frac{x+1}{x-1} \right], \quad (\text{A5})$$

$$\Pi_T(\omega, q) = \frac{1}{2}q_D^2 \left[x^2 + (1-x^2) \frac{x}{2} \log \frac{x+1}{x-1} \right], \quad (\text{A6})$$

where $x = \omega/|\mathbf{q}|$, and q_D is given by Eq. (29). Squaring Eq. (A3) we obtain

$$|\mathcal{M}_{12 \rightarrow 34}^{en}|^2 = \frac{e^4 \kappa_n^2}{4m_n^2} (|\mathcal{M}_L|^2 + |\mathcal{M}_T|^2 - 2\text{Re}[\mathcal{M}_L \mathcal{M}_T^*]), \quad (\text{A7})$$

with

$$|\mathcal{M}_L|^2 = \frac{J_e^0 J_e^{0*} J_n^0 J_n^{0*}}{|\mathbf{q}^2 + \Pi_L|^2}, \quad |\mathcal{M}_T|^2 = \frac{J_{e\perp}^i J_{e\perp}^{i*} J_{n\perp}^i J_{n\perp}^{i*}}{|\mathbf{q}^2 - \omega^2 + \Pi_T|^2}, \quad (\text{A8})$$

$$\mathcal{M}_L \mathcal{M}_T^* = \frac{J_e^0 J_{e\perp}^{i*} J_n^0 J_{n\perp}^{i*}}{(\mathbf{q}^2 + \Pi_L)(\mathbf{q}^2 - \omega^2 + \Pi_T^*)}. \quad (\text{A9})$$

After averaging over the spins, we find

$$\overline{|\mathcal{M}_L|^2} = \frac{1}{4} \sum_{\text{spins}} |\mathcal{M}_L|^2 = \frac{(16\epsilon_k \epsilon_{k'} \epsilon_p \epsilon_{p'})^{-1}}{4|\mathbf{q}^2 + \Pi_L|^2} L^{00} H^{00}, \quad (\text{A10})$$

$$\overline{|\mathcal{M}_T|^2} = \frac{1}{4} \sum_{\text{spins}} |\mathcal{M}_T|^2 = \frac{(16\epsilon_k \epsilon_{k'} \epsilon_p \epsilon_{p'})^{-1}}{4|\mathbf{q}^2 - \omega^2 + \Pi_T|^2} L_{\perp}^{ik} H_{\perp}^{ik}, \quad (\text{A11})$$

$$\overline{\mathcal{M}_L \mathcal{M}_T^*} = \frac{1}{4} \sum_{\text{spins}} \mathcal{M}_L \mathcal{M}_T^* = \frac{(16\epsilon_k \epsilon_{k'} \epsilon_p \epsilon_{p'})^{-1}}{4(\mathbf{q}^2 + \Pi_L)(\mathbf{q}^2 - \omega^2 + \Pi_T^*)} \sum_{\text{spins}} L_{\perp}^{0i} H_{\perp}^{0i}, \quad (\text{A12})$$

with the leptonic and hadronic tensors given by

$$L_{\mu\nu} = 4\epsilon_k \epsilon_{k'} \sum_{\text{spins}} J_{e\mu} J_{e\nu}^* = \text{Tr} \left[(\not{k}' + m_e) \gamma_{\mu} (\not{k} + m_e) \gamma_{\nu} \right], \quad (\text{A13})$$

$$H^{\mu\nu} = 4\epsilon_p \epsilon_{p'} \sum_{\text{spins}} J_n^{\mu} J_n^{\nu*} = \text{Tr} \left[(\not{p}' + m_n) \sigma^{\mu\rho} q_{\rho} (\not{p} + m_n) \sigma^{\nu\sigma} q_{\sigma} \right]. \quad (\text{A14})$$

Computing the traces using the standard trace algebra of Dirac matrices we find for the tensors (A13) and (A14)

$$L^{\mu\nu} = 4 [k^{\mu} k'^{\nu} + k^{\nu} k'^{\mu} - g^{\mu\nu} (k \cdot k' - m_e^2)], \quad (\text{A15})$$

$$H^{\mu\nu} = 4 \left[(q \cdot p)(q^{\mu} p'^{\nu} + q^{\nu} p'^{\mu}) + (q \cdot p')(q^{\mu} p^{\nu} + q^{\nu} p^{\mu}) - q^2 (p'^{\mu} p^{\nu} + p'^{\nu} p^{\mu}) \right. \\ \left. - 2(q \cdot p)(q \cdot p') g^{\mu\nu} \right] + 4 (m_n^2 + p \cdot p') (q^2 g^{\mu\nu} - q^{\mu} q^{\nu}), \quad (\text{A16})$$

with components of the leptonic tensor given by

$$L^{00} = 4 (\epsilon \epsilon' + \mathbf{k} \cdot \mathbf{k}' + m_e^2), \quad (\text{A17})$$

$$L_{\perp}^{0i} = 4 (\epsilon_k k_{\perp}^{'i} + \epsilon_{k'} k_{\perp}^i), \quad (\text{A18})$$

$$L_{\perp}^{ik} = 4 [k_{\perp}^i k_{\perp}^k + k_{\perp}^k k_{\perp}^i + \delta_{\perp}^{ik} (\epsilon_k \epsilon_{k'} - \mathbf{k} \cdot \mathbf{k}' - m_e^2)], \quad (\text{A19})$$

and components of the hadronic tensor given by

$$H^{00} = 8 [\omega \epsilon_{p'} (q \cdot p) + \omega \epsilon_p (q \cdot p') - q^2 \epsilon_p \epsilon_{p'} - (q \cdot p)(q \cdot p')] \\ + 4 (m_n^2 + p \cdot p') (q^2 - \omega^2), \quad (\text{A20})$$

$$H_{\perp}^{0i} = 4 [\omega (q \cdot p) - q^2 \epsilon_p] p_{\perp}^{'i} + 4 [\omega (q \cdot p') - q^2 \epsilon_{p'}] p_{\perp}^i, \quad (\text{A21})$$

$$H_{\perp}^{ik} = -4q^2 (p_{\perp}^{'i} p_{\perp}^k + p_{\perp}^{'k} p_{\perp}^i) + 4 [2(q \cdot p)(q \cdot p') - (m_n^2 + p \cdot p') q^2] \delta_{\perp}^{ik}, \quad (\text{A22})$$

where we defined $\delta_{\perp}^{ik} = \delta^{ik} - q^i q^k / q^2$. The expressions (A20)–(A22) can be simplified by using the non-relativistic limit $m_n \gg |\mathbf{p}|, |\mathbf{p}'| \simeq |\mathbf{q}|$ for neutrons. Approximating $\epsilon_p \simeq m_n^* + \mathbf{p}^2 / 2m_n$, and keeping only the leading order terms in Eqs. (A20)–(A22) we obtain

$$H^{00} \simeq 2(\mathbf{p} + \mathbf{p}')^2 q^2 - 8(\mathbf{q} \cdot \mathbf{p})(\mathbf{q} \cdot \mathbf{p}'), \quad (\text{A23})$$

$$H_{\perp}^{0i} \simeq 4m_n q^2 (p_{\perp}^i + p_{\perp}^{'i}), \quad H_{\perp}^{ik} \simeq 8m_n^2 q^2 \delta_{\perp}^{ik}. \quad (\text{A24})$$

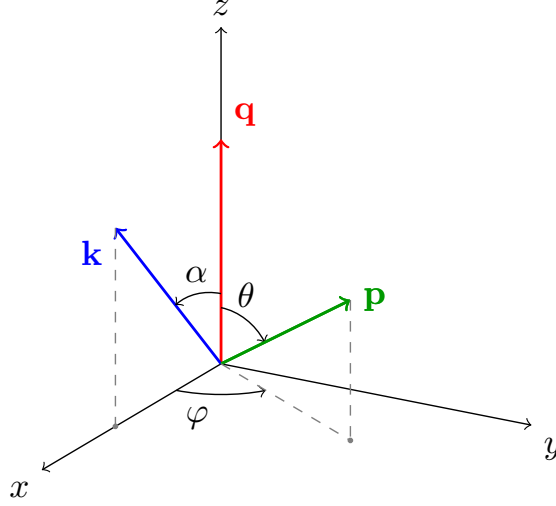


FIG. 18: The relative orientation of three vectors \mathbf{q} , \mathbf{k} and \mathbf{p} with angles defined by Eq. (A28).

Finally, by taking the ultrarelativistic limit $k, k' \gg m_e$, so that the electron energies reduce to $\epsilon_k \simeq k$ and $\epsilon_{k'} \simeq k'$, the matrix element is obtained from Eqs. (A17)–(A19) in combination with Eqs. (A23)–(A24)

$$L^{00}H^{00} = 8(kk' + \mathbf{k} \cdot \mathbf{k}') [(\mathbf{p} + \mathbf{p}')^2 q^2 - 4(\mathbf{q} \cdot \mathbf{p})(\mathbf{q} \cdot \mathbf{p}')], \quad (\text{A25})$$

$$L_{\perp}^{0i}H_{\perp}^{0i} = 32q^2m_n(k + k')(\mathbf{k}_{\perp} \cdot \mathbf{p}_{\perp}), \quad (\text{A26})$$

$$L_{\perp}^{ik}H_{\perp}^{ik} = 64q^2m_n^2(\mathbf{k}_{\perp}^2 - \mathbf{k} \cdot \mathbf{k}' + kk'), \quad (\text{A27})$$

where we used the relations $k_{\perp}^i = k_{\perp}^i$, $p_{\perp}^i = p_{\perp}^i$, and $\delta_{\perp}^{ik}\delta_{\perp}^{ik} = 2$.

To make further progress, we adopt the Cartesian system of coordinates with \mathbf{q} fixed along the z -axis, as illustrated in Fig. 18, with the angles between various vectors defined as

$$\mathbf{k} \cdot \mathbf{q} = kq \cos \alpha, \quad \mathbf{p} \cdot \mathbf{q} = pq \cos \theta, \quad \mathbf{k}_{\perp} \cdot \mathbf{p}_{\perp} = k_{\perp}p_{\perp} \cos \varphi, \quad (\text{A28})$$

$$k_{\perp} = k \sin \alpha, \quad p_{\perp} = p \sin \theta, \quad (\text{A29})$$

$$\mathbf{k} \cdot \mathbf{k}' = k^2 - kq \cos \alpha, \quad \mathbf{q} \cdot \mathbf{p}' = q^2 + pq \cos \theta, \quad (\text{A30})$$

$$(\mathbf{p} + \mathbf{p}')^2 = (2\mathbf{p} + \mathbf{q})^2 = 4p^2 + q^2 + 4pq \cos \theta, \quad (\text{A31})$$

where we used that $\mathbf{k}' = \mathbf{k} - \mathbf{q}$, $\mathbf{p}' = \mathbf{p} + \mathbf{q}$, $k' = k - \omega$. This allows us to evaluate Eqs. (A25)–(A27)

$$L^{00}H^{00} = 8q^2k(2k - \omega - q \cos \alpha)(4p^2 \sin^2 \theta + q^2), \quad (\text{A32})$$

$$L_{\perp}^{0i}H_{\perp}^{0i} = 32m_nkpq^2(2k - \omega) \sin \alpha \sin \theta \cos \varphi, \quad (\text{A33})$$

$$L_{\perp}^{ik}H_{\perp}^{ik} = 64q^2m_n^2k(k \sin^2 \alpha + q \cos \alpha - \omega), \quad (\text{A34})$$

where $q^2 \equiv |\mathbf{q}|^2$. Substituting next Eqs. (A32)–(A34) and (A10)–(A12) in Eq. (A7) we obtain

$$|\overline{\mathcal{M}}_{12 \rightarrow 34}^{en}|^2 = \frac{e^4 \kappa_n^2}{32m_n^4(k - \omega)} \left[\frac{A(\alpha, \theta)}{|q^2 + \Pi_L|^2} - \text{Re} \frac{B(\alpha, \theta) \cos \varphi}{(q^2 + \Pi_L)(q^2 - \omega^2 + \Pi_T^*)} + \frac{C(\alpha)}{|q^2 - \omega^2 + \Pi_T|^2} \right], \quad (\text{A35})$$

where the new functions in this expression are given

$$A(\alpha, \theta) = q^2(2k - \omega - q \cos \alpha)(4p^2 \sin^2 \theta + q^2), \quad (\text{A36})$$

$$B(\alpha, \theta) = 8m_npq^2(2k - \omega) \sin \alpha \sin \theta, \quad (\text{A37})$$

$$C(\alpha) = 8q^2m_n^2(k \sin^2 \alpha + q \cos \alpha - \omega). \quad (\text{A38})$$

Appendix B: Electron-neutron scattering rate

To evaluate the electron-neutron scattering rate, we start from Eq. (23) and upon introducing a dummy integration over the transferred energy $\omega = \epsilon_1 - \epsilon_3 = \epsilon_4 - \epsilon_2$, we find

$$\tau_{en}^{-1}(\epsilon) = (2\pi)^{-5} \int_{-\infty}^{\infty} d\omega \int d\mathbf{q} \int d\mathbf{p}' \overline{|\mathcal{M}_{12 \rightarrow 34}^{en}|^2} \frac{\mathbf{q} \cdot \mathbf{p}}{p^2} \delta(\epsilon - \epsilon_3 - \omega) \delta(\epsilon' - \epsilon_4 + \omega) \frac{1 - f_3^0}{1 - f_1^0} f_2'(1 - f_4'). \quad (\text{B1})$$

Note that the energies ϵ_3 and ϵ_4 should be calculated for the momentum values $\mathbf{p}_3 = \mathbf{p} - \mathbf{q}$ and $\mathbf{p}_4 = \mathbf{p}' + \mathbf{q}$, respectively, where we redefined $\mathbf{p}_1 = \mathbf{p}$, $\mathbf{p}_2 = \mathbf{p}'$, $\epsilon_1 = \epsilon$, $\epsilon_2 = \epsilon'$. Substituting the matrix element squared from Eq. (A35) into Eq. (B1) we obtain

$$\tau_{en}^{-1} = \frac{m_n}{(2\pi)^5 p} \int_{-\infty}^{\infty} d\omega \int d\mathbf{q} \cos \alpha \delta(\epsilon - \epsilon_3 - \omega) \frac{1 - f_3^0}{1 - f_1^0} \int_0^{\infty} dp' p' f_2'(1 - f_4') I_{\Omega}, \quad (\text{B2})$$

where the angular integral is given by

$$I_{\Omega} = \frac{(2\pi)e^4 \kappa_n^2}{32m_n^4(p - \omega)} \left[\frac{\tilde{A}(\alpha)}{|q^2 + \Pi_L|^2} + \frac{C(\alpha)}{|q^2 - \omega^2 + \Pi_T|^2} \right] \theta(1 - |x_0|), \quad (\text{B3})$$

with

$$\tilde{A}(\alpha) = q^2(2p - \omega - q \cos \alpha) [q^2 + 4p'^2 - 4(p'x_0)^2]. \quad (\text{B4})$$

Note that the term $\propto \cos \varphi$ vanishes upon integration.

The θ -function in Eq. (B3) defines the minimum value for p' as $|p_0|$, with $p_0 = (2\omega m_n - q^2)/2q$, which implies also $x_0 p' = p_0$. Substituting Eqs. (B3) in Eq. (B2) we obtain

$$\begin{aligned} \tau_{en}^{-1} &= \frac{e^4 \kappa_n^2}{32(2\pi)^3 m_n^2 p^2} \int_{-\infty}^{\epsilon} d\omega \frac{\epsilon - \omega}{p - \omega} \frac{1 - f^0(\epsilon - \omega)}{1 - f^0(\epsilon)} \int_0^{\infty} q dq y_0 \theta(1 - |y_0|) \\ &\times \int_{\epsilon_{\min}}^{\infty} d\epsilon' f'(\epsilon') [1 - f'(\epsilon' + \omega)] \left[\frac{\bar{A}}{|q^2 + \Pi_L|^2} + \frac{\bar{C}}{|q^2 - \omega^2 + \Pi_T|^2} \right], \end{aligned} \quad (\text{B5})$$

where we used the relation $p' dp' = m_n d\epsilon'$ and defined $\epsilon_{\min} = p_0^2/2m_n$. The functions \bar{A} and \bar{C} are given by

$$\bar{A} = q^2(2p - \omega - qy_0) (q^2 + 8m_n \epsilon' - 4p_0^2) \simeq \frac{2m_n}{\epsilon} [(2\epsilon - \omega)^2 - q^2] (2q^2 \epsilon' - \omega^2 m_n + \omega q^2), \quad (\text{B6})$$

$$\bar{C} = 8q^2 m_n^2 [p(1 - y_0^2) + qy_0 - \omega] \simeq \frac{2m_n^2}{\epsilon} [q^4 + 4q^2 \epsilon(\epsilon - \omega) - \omega^2(2\epsilon - \omega)^2], \quad (\text{B7})$$

where we substituted p_0 and y_0 and approximated $p \simeq \epsilon$ in the second step.

The θ -function in Eq. (B5) specifies the limits of integration by $q_- \leq q \leq q_+$, where $q_{\pm} = |\sqrt{(\epsilon - \omega)^2 - m^2} \pm \sqrt{\epsilon^2 - m^2}|$. To render q real, an additional condition is imposed $\omega \leq \epsilon - m_e$. Implementing these limits, we obtain

$$\begin{aligned} \tau_{en}^{-1}(\epsilon) &= \frac{\alpha^2 \kappa_n^2}{16\pi m_n \epsilon^4} \int_{-\infty}^{\epsilon - m} d\omega \frac{1 - f^0(\epsilon - \omega)}{1 - f^0(\epsilon)} \int_{q_-}^{q_+} dq (q^2 - \omega^2 + 2\epsilon\omega) \\ &\times \int_{\epsilon_{\min}}^{\infty} d\epsilon' f'(\epsilon') [1 - f'(\epsilon' + \omega)] \left[\frac{N_L}{|q^2 + \Pi_L|^2} + \frac{N_T}{|q^2 - \omega^2 + \Pi_T|^2} \right], \end{aligned} \quad (\text{B8})$$

where $e^2 = 4\pi\alpha$ and

$$N_L = [(2\epsilon - \omega)^2 - q^2] [q^2(2\epsilon' + \omega) - \omega^2 m_n], \quad (\text{B9})$$

$$N_T = m_n [q^4 + 4q^2 \epsilon(\epsilon - \omega) - \omega^2(2\epsilon - \omega)^2]. \quad (\text{B10})$$

In order to evaluate the relaxation time (B8), we first find the chemical potential from the local density of neutrons n_n , continuing to assuming $m_n^* \simeq m_n$, *i.e.*, free Fermi gas. The resulting density dependence of the neutron chemical potential at $T = 5$ MeV and $T = 10$ MeV is shown in Fig. 19. Neutrons remain non-degenerate ($T = 10$ MeV) or only semi-degenerate ($T = 5$ MeV) up to densities of order $\rho \simeq 10^{13.5} \text{ g cm}^{-3}$, becoming fully degenerate only near the

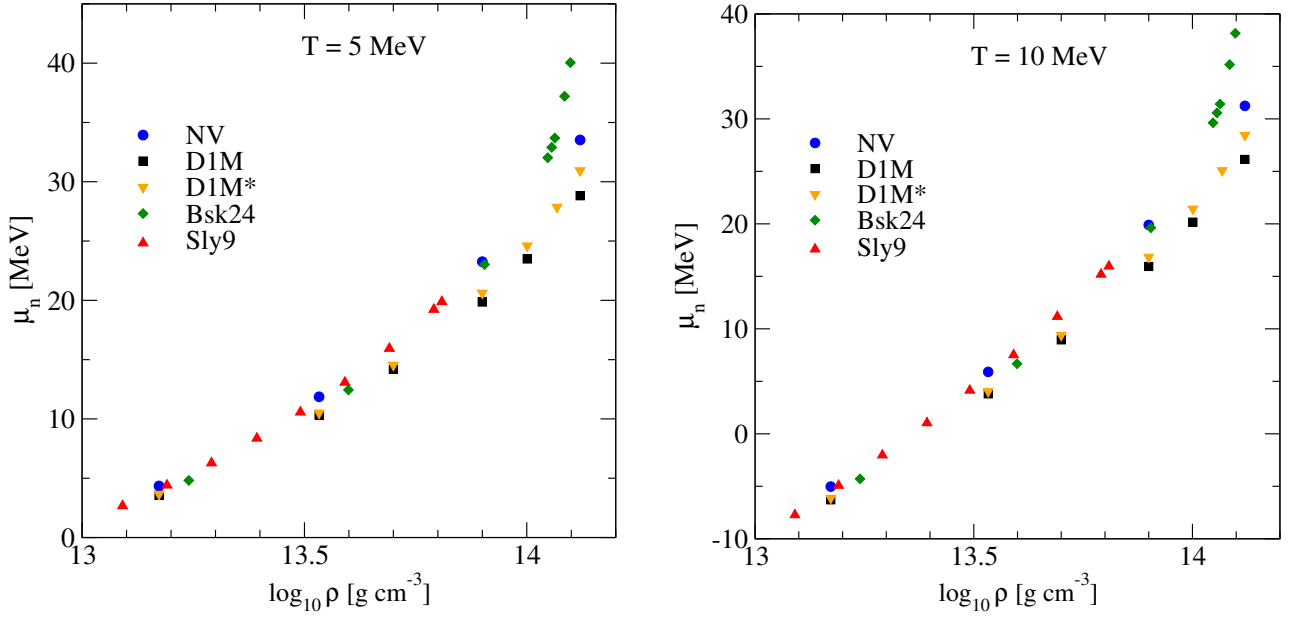


FIG. 19: The chemical potential μ_n of free neutron gas evaluated at temperature $T = 5$ MeV (left figure) and $T = 10$ MeV (right figure) as a function of density for five compositions.

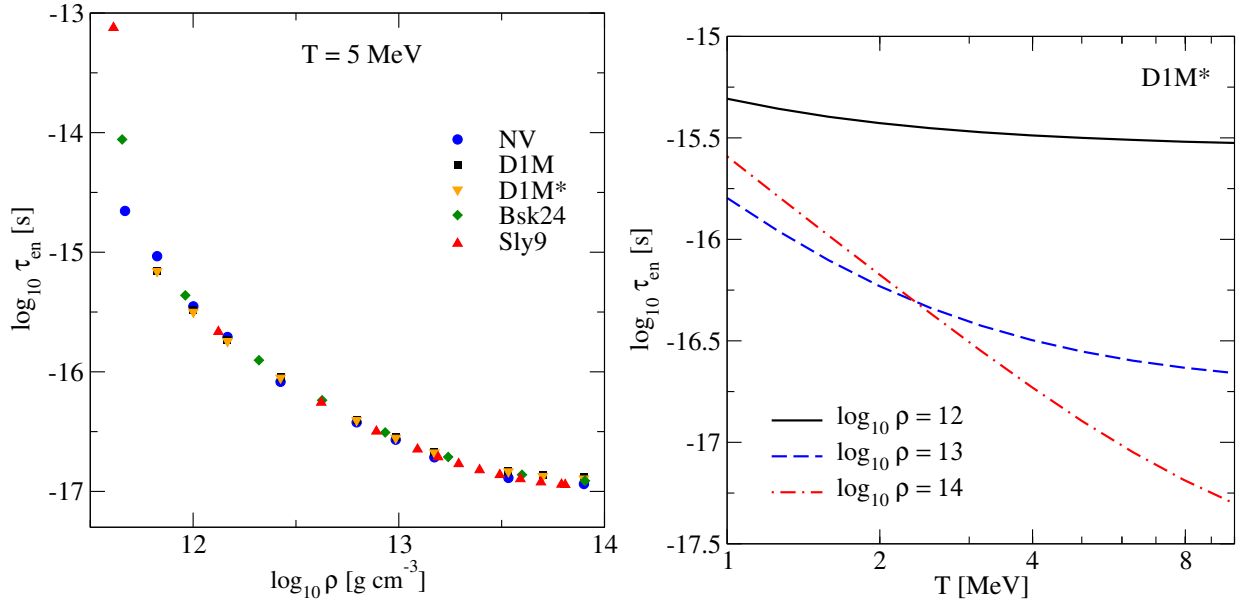


FIG. 20: Left panel: The relaxation time τ_{en} as a function of density for various compositions evaluated at temperature $T = 5$ MeV. Right panel: Dependence of relaxation time τ_{en} on temperature for various values of density for model D1M*.

bottom of the inner crust. The case $T = 1$ MeV is similar to the case $T = 5$ MeV and is not shown. At low densities, all models yield nearly identical values of μ_n . However, above densities $\rho \simeq 10^{13.5}$ g cm $^{-3}$ small differences begin to appear, growing to about 10 MeV at densities around 10^{14} g cm $^{-3}$. These deviations arise because, for compositions with smaller nuclei, the number of free neutrons in the Wigner–Seitz cell increases more rapidly than the free-neutron volume itself, resulting in larger n_n and, consequently, larger μ_n .

Figure 20 (left panel) shows the density dependence of the electron–neutron scattering relaxation time at $T = 5$ MeV. The relaxation time decreases with increasing density, in contrast to the electron–ion case. This trend simply reflects the growing free-neutron fraction at higher densities. Unlike electron–ion scattering, where the nuclear form factor

becomes important at high densities, the electron–neutron scattering rate is unaffected by any finite-size effects of the neutron. The weak dependence on the nuclear composition stems from the small variation in μ_n among the models: compositions with larger neutron chemical potentials correspond to higher neutron densities and therefore to shorter τ_{en} , as expected.

It is also worth mentioning that the main contribution to the electron-neutron scattering comes from the transverse part of the matrix element, in contrast to the electron-ion scattering. This can be seen by simply comparing Eq. (B9) and (B10), which imply $N_T \gg N_L$. This fact is not surprising, given that electron-neutron scattering is due to magnetic (*i.e.*, transverse) interaction, whereas the electron-ion scattering is mainly due to Coulomb electrostatic forces. Numerically, we find that the longitudinal part contributes only a few percent to the total electron-neutron scattering rate.

The temperature dependence of electron-neutron scattering relaxation time is shown in Fig. 20, right panel, for three different densities. The results are shown for the composition D1M*, but they are very similar also for the rest of the models. We see that the relaxation time decreases as the temperature increases, with a more significant rate of decrease at higher densities. This behavior arises mainly from the fact that an increase in temperature raises the energy ω of the transferred plasmon, resulting in higher scattering rates and, consequently, shorter relaxation times. Furthermore, at higher densities, the greater number of scattering centers for electrons leads to a more pronounced decrease in relaxation time.

Comparing Fig. 2 with the left panel of Fig. 20, we find that $\tau_{en} \gg \tau_{ei}$ throughout the entire inner crust, with the smallest ratio $\tau_{en}/\tau_{ei} \sim 10^2$ occurring in the densest layers. Consequently, electron–neutron scattering has a negligible impact on electron transport across the entire crust. An analogous conclusion was reached in Ref. [1] for cold neutron-star matter in the solid phase.

Appendix C: Low-temperature limit of transport coefficients

To derive the low-temperature counterparts of the transport coefficients, we use the well-known expansion formula for $T \ll T_F$ Eq. (7.83)]

$$\int_m^\infty d\epsilon \frac{\partial f^0}{\partial \epsilon} F(\epsilon) = -F(\mu) - \frac{\pi^2 T^2}{6} F''(\mu) + \mathcal{O}(T^4), \quad (\text{C1})$$

where $F(\epsilon)$ is a well-behaved function around $\epsilon = \mu$ and prime denotes derivative with respect to ϵ . For the tensor in Eq. (37) with $n = 0$ it is sufficient to keep the first term with $\mu \approx \epsilon_F$, whereas for the tensors with $n = 1, 2$ the first term vanishes, and the leading order term is $\mathcal{O}(T^2)$. Thus one finds

$$\mathcal{L}_l^0 = \frac{1}{3\pi^2} \mathcal{F}_l(\epsilon_F), \quad \mathcal{L}_l^1 = \frac{T}{9} \mathcal{F}_l'(\epsilon_F), \quad \mathcal{L}_l^2 = \frac{1}{9} \mathcal{F}_l(\epsilon_F). \quad (\text{C2})$$

In order to evaluate the derivative $\mathcal{F}_l'(\epsilon)$ we use that $p \simeq \epsilon$, $\tau \propto \epsilon^2$ [18], $\omega_c \propto \epsilon^{-1}$, therefore $\tau' = 2\tau/\epsilon$, $(\omega_c \tau)' = \omega_c \tau/\epsilon$, therefore,

$$\mathcal{F}'(\epsilon) = \frac{d}{d\epsilon} \left(\frac{p^3}{\epsilon} \tau \right) = 4p\tau, \quad (\text{C3})$$

$$\mathcal{F}_0'(\epsilon) = \frac{d}{d\epsilon} \left[\frac{p^3}{\epsilon} \frac{\tau}{1 + (\omega_c \tau)^2} \right] = 2p\tau \frac{2 + (\omega_c \tau)^2}{[1 + (\omega_c \tau)^2]^2}, \quad (\text{C4})$$

$$\mathcal{F}_1'(\epsilon) = \frac{d}{d\epsilon} \left[\frac{p^3}{\epsilon} \frac{\tau(\omega_c \tau)}{1 + (\omega_c \tau)^2} \right] = p\omega_c \tau^2 \frac{5 + 3(\omega_c \tau)^2}{[1 + (\omega_c \tau)^2]^2}. \quad (\text{C5})$$

Eqs. (37) and (C2) lead to the limiting forms of the components of the electrical conductivity tensor

$$\sigma_l = \frac{e^2}{3\pi^2} \mathcal{F}_l(\epsilon_F) = \frac{e^2}{3\pi^2} \frac{p_F^3}{\epsilon_F} \tau_F \frac{(\omega_{cF} \tau_F)^l}{1 + (\omega_{cF} \tau_F)^2} = \frac{n_e e^2 \tau_F}{\epsilon_F} \frac{(\omega_{cF} \tau_F)^l}{1 + (\omega_{cF} \tau_F)^2}, \quad (\text{C6})$$

$$\sigma = \frac{n_e e^2 \tau_F}{\epsilon_F}, \quad \sigma_0 = \frac{\sigma}{1 + (\omega_{cF} \tau_F)^2}, \quad \sigma_1 = \frac{\omega_{cF} \tau_F}{1 + (\omega_{cF} \tau_F)^2} \sigma, \quad (\text{C7})$$

where we used the relation $p_F^3 = 3\pi^2 n_e$ and defined $\omega_{cF} = \omega_c(\epsilon_F)$, $\tau_F = \tau(\epsilon_F)$. The first expression in Eq. (C7) is the well-known Drude formula. For $\tilde{\kappa}_l$ and α_l we find from Eq. (37)

$$\tilde{\kappa}_l = \frac{T}{9} \mathcal{F}_l(\epsilon_F) = \frac{\pi^2}{3e^2} T \sigma_l, \quad \alpha_l = -\frac{eT}{9} \mathcal{F}_l'(\epsilon_F), \quad (\text{C8})$$

and, using Eqs. (C3)–(C5),

$$\tilde{\kappa} = \frac{\pi^2 n_e \tau_F}{3\epsilon_F} T, \quad \tilde{\kappa}_0 = \frac{\tilde{\kappa}}{1 + (\omega_{cF} \tau_F)^2}, \quad \tilde{\kappa}_1 = \frac{\omega_{cF} \tau_F}{1 + (\omega_{cF} \tau_F)^2} \tilde{\kappa}. \quad (\text{C9})$$

For α_l we find

$$\alpha = -\frac{eT}{9}(3 + v_F^2)p_F \tau_F = -\frac{4eT}{9}p_F \tau_F, \quad (\text{C10})$$

$$\alpha_0 = -\frac{eT}{9}p_F \frac{\tau_F}{1 + (\omega_{cF} \tau_F)^2} \left[2 + \frac{2}{1 + (\omega_{cF} \tau_F)^2} \right], \quad (\text{C11})$$

$$\alpha_1 = -\frac{eT}{9}p_F \frac{\tau_F (\omega_{cF} \tau_F)}{1 + (\omega_{cF} \tau_F)^2} \left[3 + \frac{2}{1 + (\omega_{cF} \tau_F)^2} \right]. \quad (\text{C12})$$

From Eqs. (C7) for the components of the conductivity we obtain the relation

$$\sigma_0^2 + \sigma_1^2 = \left\{ \frac{1}{[1 + (\omega_{cF} \tau_F)^2]^2} + \frac{(\omega_{cF} \tau_F)^2}{[1 + (\omega_{cF} \tau_F)^2]^2} \right\} \sigma^2 = \frac{\sigma^2}{1 + (\omega_{cF} \tau_F)^2} = \sigma \sigma_0, \quad (\text{C13})$$

whereas for the components of thermopower Q using Eqs. (42) and (C10)–(C12) we find

$$Q = \frac{4\pi^2 T}{3e\epsilon_F}, \quad Q_0 = \frac{\pi^2 T}{3e\epsilon_F} \left[3 + \frac{1}{1 + (\omega_{cF} \tau_F)^2} \right], \quad Q_1 = \frac{\pi^2 T}{3e\epsilon_F} \frac{(\omega_{cF} \tau_F)}{1 + (\omega_{cF} \tau_F)^2}. \quad (\text{C14})$$

For small values of the Hall parameter $\omega_{cF} \tau_F \ll 1$ one then finds

$$Q_0 \simeq Q, \quad Q_1 \simeq \frac{\pi^2 T}{3e\epsilon_F} (\omega_{cF} \tau_F) = \frac{\pi^2 \tau_F}{3\epsilon_F^2} T B = \frac{1}{4} (\omega_{cF} \tau_F) Q \ll Q, \quad (\text{C15})$$

whereas in the opposite limit $\omega_{cF} \tau_F \gg 1$

$$Q_0 \simeq \frac{p_F \epsilon_F}{3n_e e} T = \frac{3Q}{4}, \quad Q_1 \simeq \frac{\pi^2 T}{3e\epsilon_F} \frac{1}{\omega_{cF} \tau_F} = -\frac{\pi^2}{3e^2 \tau_F} \frac{T}{B} = \frac{1}{4} \frac{Q}{\omega_{cF} \tau_F} \ll Q. \quad (\text{C16})$$

Using Eqs. (43)–(45) and (C9)–(C14), for the thermal conductivity in the low- T limit we find $\hat{\kappa} \simeq \hat{\tilde{\kappa}}$. From Eq. (C8) we recover the Wiedemann-Franz law for low-temperature (degenerate) materials: $(3e^2 \kappa)/(\pi^2 \sigma T) \rightarrow 1$. For $\omega_{cF} \tau_F \ll 1$ one finds

$$\kappa_0 \simeq \kappa, \quad \kappa_1 \simeq (\omega_{cF} \tau_F) \kappa = \frac{\pi^2 n_e e \tau_F^2}{3\epsilon_F^2} T B \simeq \frac{3eB}{\pi^2 n_e T} \kappa^2, \quad (\text{C17})$$

and for $\omega_{cF} \tau_F \gg 1$

$$\kappa_0 \simeq \frac{\kappa}{(\omega_{cF} \tau_F)^2} = \frac{\pi^2 n_e \epsilon_F}{3e^2 \tau_F} \frac{T}{B^2} = \left(\frac{\pi^2 n_e T}{3eB} \right)^2 \kappa^{-1}, \quad \kappa_1 \simeq \frac{\kappa}{\omega_{cF} \tau_F} = \frac{\pi^2 n_e T}{3eB}. \quad (\text{C18})$$

-
- [1] E. Flowers and N. Itoh, *Transport properties of dense matter*, *ApJ* **206** (1976) 218–242.
 - [2] D. G. Yakovlev and V. A. Urpin, *Thermal and Electrical Conductivity in White Dwarfs and Neutron Stars*, *Soviet Ast.* **24** (1980) 303.
 - [3] V. A. Urpin and D. G. Yakovlev, *Thermogalvanomagnetic Effects in White Dwarfs and Neutron Stars*, *Soviet Ast.* **24** (1980) 425.

-
- [4] E. Flowers and N. Itoh, *Transport properties of dense matter. III - Analytic formulae for thermal conductivity*, *ApJ* **250** (1981) 750–752.
 - [5] N. Itoh, S. Mitake, H. Iyetomi and S. Ichimaru, *Electrical and thermal conductivities of dense matter in the liquid metal phase. I - High-temperature results*, *ApJ* **273** (1983) 774–782.
 - [6] N. Itoh, Y. Kohyama, N. Matsumoto and M. Seki,

- Electrical and Thermal Conductivities of Dense...*, *ApJ* **285** (1984) 758.
- [7] R. Nandkumar and C. J. Pethick, *Transport coefficients of dense matter in the liquid metal regime*, *MNRAS* **209** (1984) 511–524.
- [8] D. M. Sedrakian and A. K. Avetisyan, *Magnetohydrodynamics of plasma in the crust of a neutron star*, *Astrofizika* **26** (1987) 489–500.
- [9] N. Itoh and Y. Kohyama, *Electrical and Thermal Conductivities of Dense Matter in the Crystalline Lattice Phase. II. Impurity Scattering*, *ApJ* **404** (1993) 268.
- [10] D. A. Baiko, A. D. Kaminker, A. Y. Potekhin and D. G. Yakovlev, *Ion Structure Factors and Electron Transport in Dense Coulomb Plasmas*, *Phys. Rev. Lett.* **81** (1998) 5556–5559, [physics/9811052].
- [11] A. Y. Potekhin, *Electron conduction in magnetized neutron star envelopes*, *A&A* **351** (1999) 787–797.
- [12] P. S. Shternin and D. G. Yakovlev, *Electron thermal conductivity owing to collisions between degenerate electrons*, *Phys. Rev. D* **74** (2006) 043004, [astro-ph/0608371].
- [13] N. Itoh, S. Uchida, Y. Sakamoto, Y. Kohyama and S. Nozawa, *The Second Born Corrections to the Electrical and Thermal Conductivities of Dense Matter in the Liquid Metal Phase*, *ApJ* **677** (2008) 495–502, [0708.2967].
- [14] A. Schmitt and P. Shternin, *Reaction Rates and Transport in Neutron Stars*, in *Astrophysics and Space Science Library* (L. Rezzolla, P. Pizzochero, D. I. Jones, N. Rea and I. Vidaña, eds.), vol. 457 of *Astrophysics and Space Science Library*, p. 455, Springer, New York, 2018. DOI.
- [15] A. Y. Potekhin, J. A. Pons and D. Page, *Neutron Stars—Cooling and Transport*, *Space Sci. Rev.* **191** (2015) 239–291, [1507.06186].
- [16] G. S. Bisnovatyi-Kogan and M. M. Romanova, *Diffusion and thermal transfer of neutrons in solid envelopes of neutron stars*, *Zhurnal Eksperimentalnoi i Teoreticheskoi Fiziki* **83** (1982) 449–459.
- [17] A. Harutyunyan, A. Sedrakian, N. T. Gevorgyan and M. V. Hayrapetyan, *Electrical conductivity of a warm neutron star crust in magnetic fields: Neutron-drip regime*, *Phys. Rev. C* **109** (2024) 055804, [2309.00893].
- [18] A. Harutyunyan and A. Sedrakian, *Electrical conductivity of a warm neutron star crust in magnetic fields*, *Phys. Rev. C* **94** (2016) 025805.
- [19] A. Harutyunyan and A. Sedrakian, *Thermal Conductivity and Thermal Hall Effect in Dense Electron-Ion Plasma*, *Particles* **7** (2024) 967–983, [2409.01304].
- [20] A. Harutyunyan, A. Nathanail, L. Rezzolla and A. Sedrakian, *Electrical resistivity and Hall effect in binary neutron star mergers*, *European Physical Journal A* **54** (2018) 191.
- [21] E. Flowers and N. Itoh, *Transport properties of dense matter. II.*, *ApJ* **230** (1979) 847–858.
- [22] B. Bertoni, S. Reddy and E. Rrapaj, *Electron-neutron scattering and transport properties of neutron stars*, *Phys. Rev. C* **91** (2015) 025806, [1409.7750].
- [23] A. Z. Dolginov and V. A. Urpin, *The Thermomagnetic Instability in Degenerate Cores of White Dwarfs*, *Ap&SS* **69** (1980) 259–267.
- [24] R. D. Blandford, J. H. Applegate and L. Hernquist, *Thermal origin of neutron star magnetic fields.*, *MNRAS* **204** (1983) 1025–1048.
- [25] U. Geppert and H. J. Wiebicke, *Amplification of neutron star magnetic fields by thermoelectric effects. I - General formalism*, *A&AS* **87** (1991) 217–228.
- [26] H. J. Wiebicke and U. Geppert, *Amplification of neutron star magnetic fields by thermoelectric effects. VI. Analytical approach.*, *A&A* **309** (1996) 203–212.
- [27] D. Gakis and K. N. Gourgouliatos, *Revisiting thermoelectric effects in the crust of neutron stars*, *A&A* **690** (2024) A117, [2402.14911].
- [28] A. D. Kaminker, D. G. Yakovlev, A. Y. Potekhin, N. Shibasaki, P. S. Shternin and O. Y. Gnedin, *Magnetars as cooling neutron stars with internal heating*, *MNRAS* **371** (2006) 477–483, [astro-ph/0605449].
- [29] U. Geppert, *Magneto-Thermal Evolution of Neutron Stars with Emphasis to Radio Pulsars*, *Journal of Astrophysics and Astronomy* **38** (2017) 46, [1709.08005].
- [30] C. Dehman, D. Viganò, J. A. Pons and N. Rea, *3D code for Magneto-Thermal evolution in Isolated Neutron Stars, MATINS: the magnetic field formalism*, *MNRAS* **518** (2023) 1222–1242, [2209.12920].
- [31] S. Ascenzi, D. Viganò, C. Dehman, J. A. Pons, N. Rea and R. Perna, *3D code for Magneto-Thermal evolution in Isolated Neutron Stars, MATINS: thermal evolution and light curves*, *MNRAS* **533** (2024) 201–224, [2401.15711].
- [32] J. W. Negele and D. Vautherin, *Neutron star matter at sub-nuclear densities*, *Nucl. Physics, Sect. A* **207** (1973) 298–320.
- [33] C. Mondal, X. Viñas, M. Centelles and J. N. De, *Structure and composition of the inner crust of neutron stars from gogny interactions*, *Phys. Rev. C* **102** (2020) 015802.
- [34] J. M. Pearson, N. Chamel, A. Y. Potekhin, A. F. Fantina, C. Ducoin, A. K. Dutta et al., *Unified equations of state for cold non-accreting neutron stars with Brussels-Montreal functionals - I. Role of symmetry energy*, *MNRAS* **481** (2018) 2994–3026, [1903.04981].
- [35] A. R. Raduta and F. Gulminelli, *Nuclear Statistical Equilibrium equation of state for core collapse*, *Nucl. Phys. A* **983** (2019) 252–275.
- [36] E. Braaten and R. D. Pisarski, *Soft Amplitudes in Hot Gauge Theories: A General Analysis*, *Nucl. Phys. B* **337** (1990) 569–634.
- [37] E. Braaten and R. D. Pisarski, *Simple effective Lagrangian for hard thermal loops*, *Phys. Rev. D* **45** (1992) R1827.
- [38] G. Baym, H. A. Bethe and C. J. Pethick, *Neutron star matter*, *Nucl. Phys. A* **175** (1971) 225–271.
- [39] N. Itoh, Y. Kohyama, N. Matsumoto and M. Seki, *Electrical and thermal conductivities of dense matter in the crystalline lattice phase*, *ApJ* **285** (1984) 758–765.
- [40] S. Galam and J.-P. Hansen, *Statistical mechanics of dense ionized matter. VI. Electron screening corrections to the thermodynamic properties of the one-component plasma*, *Phys. Rev. A* **14** (1976) 816–832.
- [41] M. N. Tamashiro, Y. Levin and M. C. Barbosa, *The one-component plasma: a conceptual approach*, *Physica A Statistical Mechanics and its Applications* **268** (1999) 24–49, [cond-mat/9810213].